ORIGINAL ARTICLE

Wulff Possart · Bettina Zimmer

Water in polyurethane networks: physical and chemical ageing effects and mechanical parameters

Abstract The chemical structure, polymer mobility and mechanical properties are studied for a cross-linked amorphous poly(ether urethane) (PU) from glass transition to rubber elasticity for juvenile dry samples and for water-saturated states after exposure to humid air (r.h. = 29, 67, 95, 100%) at 60 °C during 1 y of ageing. For saturated samples, network chain cleavage is the *chemical ageing mechanism,* but it is too weak and slow to affect on the physical properties significantly within 1 y. Water acts primarily in a physical manner. Within 1 d, H_2O molecules replace part of the weak urethane H-bonds by H_2O–urethane H-bonds and reduce all other physical interactions between network chains by solvating hydrophilic segments. Thus, the cooperative polymer mobility strongly amplifies: The gain of specific conformational entropy doubles across the caloric glass transition, which shifts by -17 K. A H_2O concentration of only $c_{H_2O} \approx (0.4 \ldots 0.5) \, c_{H_2O,max}$ suffices for the major part of these fast rearrangements. Some part of the water slowly forms (during 3–4 months) a finely dispersed water-rich mixed phase with the PU chains. Except the new phase, these molecular processes of *physical ageing* strongly affect the mechanical properties at damage-free deformation. For dry PU in the glass transition, the shear modulus, $\mu_{relaxed}(T)$, after viscoelastic stress relaxation only depends on the deformation-induced entropy change—like in the rubber elastic state. Within one month, water drastically decreases the *viscoelastic* response, as expected for plasticisation. However, $\mu_{relaxed}(T)$ slightly *grows* in wet PU. H_2O molecules cause these opposite trends by boosting the cooperative mobility (i.e. extension of the accessible conformational space and entropy by reduction in energy barriers) and by occupation of free volume compartments. Water quickly reduces the fracture parameters by about 50%. We explain that embrittlement by the H_2O-induced facilitation of cooperative network chain motions, which let fracture proceed with less energy. In summary, our findings provide a detailed conception of the molecular effects the H_2O molecules have on the PU network, and they explain the consequences for the mechanical properties.

Keywords Polyurethane · Water uptake · Moist–warm ageing · Chemical ageing · Physical ageing · Mechanical modulus · Fracture parameters

Abbreviations

PU	Polyurethane, here cross-linked amorphous poly(ether urethane)
r.h.	Relative humidity

W. Possart (✉)
Former Chair for Adhesion and Interphases in Polymers, Saarland University, Campus, 66123 Saarbrücken, Germany
E-mail: w.possart@mx.uni-saarland.de

B. Zimmer
Goethestraße 22, 66386 St. Ingbert, Germany

y	Year
d	Day
H-bond	Hydrogen bond
IR	Infrared
ATR	Attenuated total refection
DSC	Differential scanning calorimetry
MDI	Methylene diphenyl diisocyanate or diphenyl methane diisocyanate
PTFE	Poly(tetra fluoro ethylene)
OH-group	Hydroxyl group
NCO-group	Isocyanate group
h	Hour
FTIR	Fourier transform infrared spectroscopy
ZnSe	Zinc selenide
MCT	Mercury cadmium telluride, a common material for IR detectors
T-rate	Temperature rate for heating and cooling, respectively
GT^{cal}	Caloric glass transition
GAB	Guggenheim, Anderson, de Boer

1 Introduction

Water is present in numerous applications of polymer materials. It is one of the factors contributing to the ageing of polymers, and it causes significant changes of the mechanical properties. In many polymers, water causes plasticisation. Therefore, understanding of the fundamental mechanisms of plasticisation is of interest. For the large group of the technologically most important polyurethane (PU) materials, knowledge on the ageing mechanisms on a molecular level, particularly on the impact of water, and on their effect on macroscopic material properties is still incomplete (cf. e.g. [1–9]). In the literature, studies sometimes miss important details like chemical composition, morphology or glass transition of the examined PU (e.g. [1,4,7,9–16]). Other publications focus on chemical ageing effects but do not consider the consequences on macroscopic material properties (e.g. [2,3,17–21]). Concerning the role of water, papers like [5,6,22,23] describe quantitative aspects but very many (e.g. [1,4,7,9–16,24–28]) are content with a qualitative description. Cross-linked PUs are much less studied than thermoplastic PUs. In conclusion, the state of the art on ageing of PU materials is coined by an incomplete understanding of the basic mechanisms and their implication on structure and physical properties (cf. also the recent reviews [29,30]).

This paper considers a cross-linked amorphous PU of well-defined chemical structure and physical state. Covering the range from the glass transition temperature to the rubber elastic state, the study characterises the PU in its initial state and during ageing under moderate conditions (T_{age} = 60 °C, humid air) with respect to chemical structure, macromolecular mobility and mechanical properties, including fracture. The experimental findings provide a detailed conception of the effects the H_2O molecules have on the molecular interactions (hydrogen bonds) and on the cooperative polymer dynamics, and they explain the consequences for the mechanical properties.

2 Materials and methods

2.1 Polymer sample preparation and ageing conditions

2.1.1 Monomers

Three commercial monomers (Covestro, Germany) form the reactive system—Fig. 1: an oligo etherdiol ('Diol', Desmophen 3600Z), an oligo ethertriol ('Triol', Baygal K55) and diphenyl methane diisocyanate ('MDI', Desmodur VP.PU 1806).

The quite long Diol molecules provide for chain mobility due to the oligo ether sequence, while the Triol molecules form the cross-links in the amorphous PU network. Due to their hygroscopicity, Diol and Triol come with a little content of water ($\leq$ 0.05 wt%) and have to be handled in dry atmosphere [31–34]. The mix of MDI isomers avoids crystallisation, but a dry atmosphere is mandatory for this monomer as well because of the high reactivity of the isocyanate group ($-N=C=O$) with H_2O which would give unwanted urea
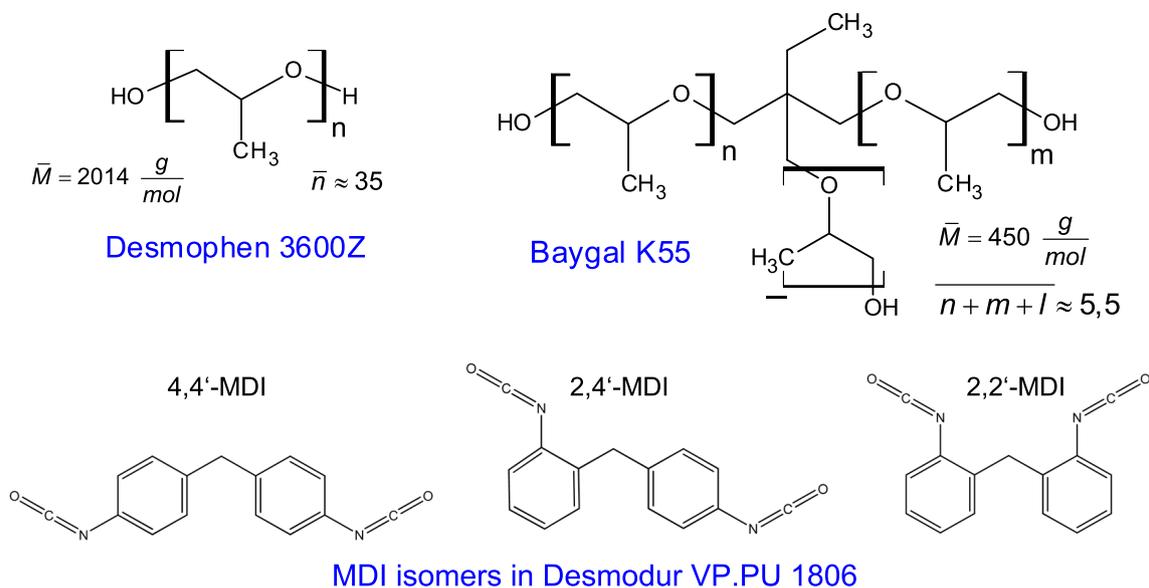
Fig. 1 Chemical structures of the monomers for the PU network

groups in the forming network. Thanks to low viscosity, all three monomers mix easily by a magnetic stirrer at room temperature. A glove box purged with dried air (rel. humidity r. h. = 0.07% at 23 °C, i.e. abs. hum. of $\sim 1.6 \cdot 10^{-5}$ mol H_2O / mol air) provides the dry conditions for storage and sample preparation.

2.1.2 Sample preparation

The Diol–Triol ratio is chosen to give a molar ratio of $OH_{triol}/OH_{diol} = 90 : 10$. With a stoichiometric concentration of isocyanate groups from the MDI, the resulting polyurethane 'PU9010' possesses good mechanical properties and a caloric glass transition around room temperature. The reactive monomers are mixed at room temperature in a glove box (air, r. h. = 0.07%) by five steps: i. mixing of appropriate masses of Diol and Triol by a magnetic stirrer for 15 min; ii. degassing of the homogeneous alcohol mixture under vacuum for 10 min. in order to remove dispersed air; iii. slow addition of the appropriate mass of MDI under constant stirring; iv. homogenisation of the reaction batch by another 15 min. of stirring; and v. final vacuum degassing for 15 min. for the removal of dispersed air and of traces of CO_2—the reaction product of isocyanate groups with the little water content in the monomers (see above). Specimens (for dimensions see below) are cast in PTFE moulds from the batch right after preparation (inside the glove box under dried air).

Because this formulation is applied as a room-temperature curing material in practice, the first step of chemical cross-linking runs at room temperature (23−25 °C) for 7 days. However, the resulting network is imperfect because the batch vitrifies chemically before ultimate conversion of reactive OH- and NCO-groups. The chemical reactions of these residual groups during ageing would compromise the ageing mechanisms of the PU network itself. Hence, a post-curing step follows at 60 °C (i.e. above the final glass transition) for another 7 days providing the fully cross-linked PU with the maximum concentration of urethane groups.

These chemically and structurally well-defined PU9010 specimens are stored in the glove box in dried air (r. h. = 0.07%) at 23 °C until characterisation or ageing in moist air. That protocol warrants a dry and stable initial state of the specimens ('juvenile' samples).

2.1.3 Ageing regimes

Free-standing samples age at constant 60 °C in humid air (r. h. = const. = 'dried' or 29, 67, 95, 100% corresponding to absolute humidity levels of $1.6 \cdot 10^{-5} \approx 0$ or $6.1 \cdot 10^{-2}, 1.5 \cdot 10^{-1}, 2.3 \cdot 10^{-1}, 2.4 \cdot 10^{-1}$ mol H_2O/mol air) for up to 1 year. Such conditions seem to be mild, but they are close to the limits recommended for application of such PU networks. More important, the moderate temperature avoids specific high-temperature processes, which do not occur in the material under real conditions.

Table 1 ATR measurements—conditions and parameters. The angle of incidence is well above the critical angle of total reflectance for PU9010

Temperature	Room temperature
Atmosphere	Dried air (r. h. = 0.07%)
ATR element	ZnSe hemisphere
Sample contact force	Not calibrated
IR source	Globar
Detector type	MCT
Aperture	2 mm
Spectral region, resolution	4000–700 cm^{-1} (mid IR), 4 cm^{-1}
Angle of incidence	60°
Polarisation of light	p-polarised
Number of scans	500

After selected ageing times, the samples are transferred in moist environment to the characterisation experiment in order to avoid re-drying of the polymer during transport.

Occasionally, aged samples re-dry in the glove box to see if the absorbed water left permanent property changes.

2.2 Characterisation methods

2.3 Gravimetry for water uptake

Flat plates (length $\times$ width = 9 $\times$ 3 cm^2) of fully cured PU9010 serve as specimens for the water uptake measurements. Plate thickness, d_P, is $\sim$2 mm as measured for each specimen by a micrometre gauge (resolution 1 μm). The small thickness as compared to sample length and width warrants a manageable time scale for water uptake, and it makes the one-dimensional transport a very good approximation for water absorption and desorption.

After selected exposure times to humid air (cf. Sect. 2.1, ageing regimes), the sample is weighed at room temperature in laboratory atmosphere (r. h. $\sim$35%) with a precision scale (ABJ 320-4, Kern & Sohn GmbH, Germany, resol. 0.1 mg, accuracy 0.2 mg, [35]). For a given water uptake, three samples are scaled to get an average value. The measuring time is minimised to about 5 min. in order to prevent re-drying as much as possible. Then, samples return to the ageing vessel where they stay for at least 3 h before next weighing. This period compensates for the little fluctuations of temperature and water content in the ageing vessel due to sample removal and return [36].

2.4 Infrared spectroscopy for chemical structure

The FTIR spectrometers IFS 66v/S and Vertex 70v (Bruker, Germany) served for the ATR (attenuated total reflection) measurements at room temperature. For good optical contact, a force presses the ATR element on the sample. For the aged samples, this close contact also avoids re-drying during recording a spectrum. Table 1 provides the measuring conditions and parameters.

Specimens ($\sim$5 mm $\times$ 5 mm) are cut from the PU9010 plates for spectral characterisation. The IR beam diameter (2 mm) and the angle of incidence determine the monitored sample area. The information depth of IR-ATR-spectra depends on light incidence and wave number, on the refractive index of the ATR element, and on the optical function (i.e. refractive index and absorption of light as functions of frequency) of the PU. For the conditions given, the upper limit of the information depth ranges approx. from 250 nm to 1.2 μm for transparent spectral regions of PU9010. The information depth gets smaller with increasing light absorption, but we proved on cross sections of juvenile samples that the ATR spectra display the chemical situation in the bulk material.

2.4.1 Differential scanning calorimetry (DSC) for thermal transitions

DSC was carried out on a Q100 (TA Instruments, Eschborn, Germany). Cylindrical samples (5.7 $\pm$ 0.2 mg, diameter $\sim$2 mm, thickness $\sim$1 mm) cut from PU9010 sheets are placed in the centre of the aluminium DSC

Table 2 Measuring protocol for the caloric characterisation. T-rate = constant rate for heating and cooling, T_{end} = final temperature for a heating or cooling step, respectively, t_{hold} = time for temperature equilibration after a heating or cooling step

Step	Regime	T-rate	T_{end}	t_{hold} at T_{end}
1	Cool	-10 K/min	-75 °C	10 min
2	Heat	$+10$ K/min	125 °C	10 min
3	Cool	-10 K/min	-75 °C	10 min
4	Heat	$+10$ K/min	125 °C	10 min
5	Cool	-10 K/min	-75 °C	10 min
6	Heat	$+10$ K/min	125 °C	10 min
7	Cool	-10 K/min	-75 °C	–

pans. A lid with a hole for isobaric measurements seals the pan. Pan and lid contact the sample closely for the best possible heat transfer. A gold layer on the inner surface of pan and lid avoids reactions with the sample. Purging with pure nitrogen gas (20 ml/min) maintains dry, chemically inert conditions during measurement. The measuring protocol starts at room temperature and comprises three cycles of cooling and heating as described in Table 2.

The maximum temperature of 125 °C regards the thermal stability of the PU, particularly of the urethane groups. Note that the DSC device attains constant heating rates only above -60 °C.

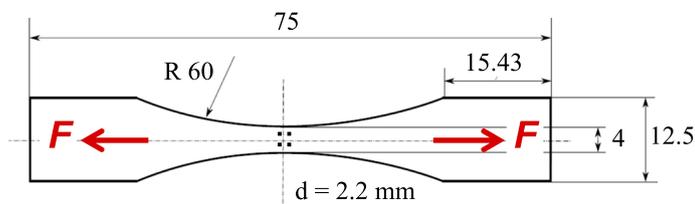### 2.4.2 Mechanical characterisation by uniaxial isothermal tensile tests

A Kappa 20 testing machine (ZwickRoell GmbH & Co. KG, Germany) serves for these experiments—cf. Table 3 for the technical data and the experimental parameters.
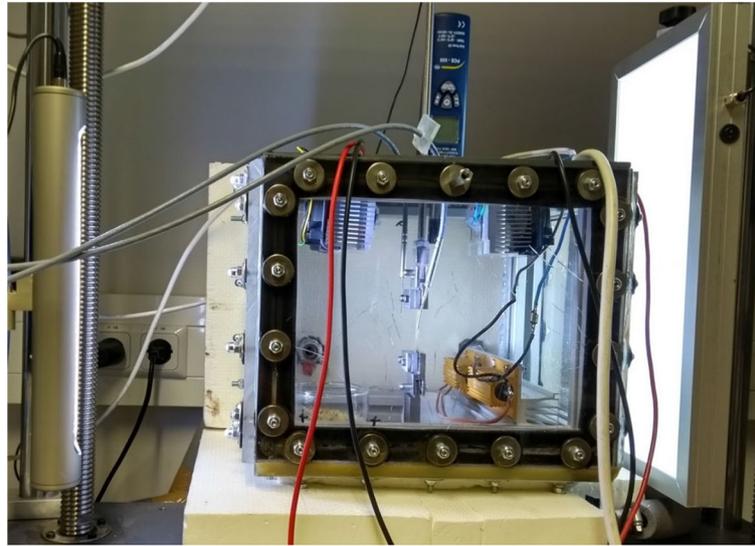
The waisted dog bone-shaped specimens (see Fig. 2 for geometry, thickness (2.2 ± 0.2) mm) cure at room temperature in PTFE moulds. After removal, the free samples post-cure at 60 °C on a flat PTFE surface in order to minimise residual mechanical stresses.

Due to the waisted shape, the cross-sectional area decreases primarily close to the centre of the specimen such that the tensile stress under load, F, is maximal in the region where the video extensometry markers are. Thus, the video extensometer monitors the evolving longitudinal and transverse stretches, λ_1 and λ_2,
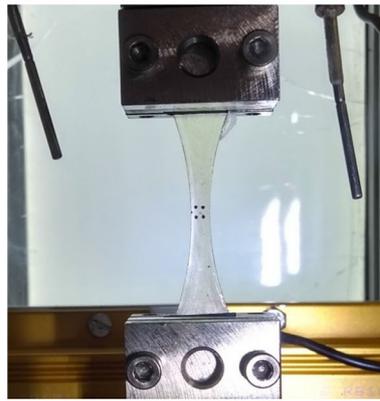
Table 3 Technical data of the testing system and conditions for the uniaxial tensile tests. For the given test temperature, T_{test}, the r. h. is adapted to reproduce the chemical potential, μ_{H_2O}, water has during ageing at 60 °C such that the sample water content is stable during the mechanical test

Force sensor	KD24s, $\pm (200 \pm 0.2)$ N (ME-Meßsysteme, Germany)
Video extensometer for local stretch	VideoXtens, objective Tamron 1A1HB F 3.9/75 mm
Testing conditions—dried samples:	Dried air at $T_{test} = 26$ °C or
	40 °C or
	60 °C
Testing conditions—aged samples:	Air at
•aged at 29% r. h.:	•26 °C, (50 ± 2)% r. h.
•aged at 67% r. h.:	•26 °C, (44 ± 6)% r. h.
•aged at 100% r. h.:	•26 °C, (87 ± 3)% r. h. or
	40 °C, (83 ± 4)% r. h. or
	60 °C, (79 ± 5)% r. h.

Fig. 2 Waisted dog bone sample geometry (adapted from [37]) for the mechanical tests. F = force response in the test. The four black dots around the sample centre are the markers for the video extensometry. Marker diameter and distance: 1 mm and 2 mm, respectively

(a)

(b)

Fig. 3 a Experimental set-up with the customised box on the Kappa 20 (after [39]). The camera for the video extensometry is located beyond the left margin of the image. **b** Mounted dog bone specimen with the four black markers for video extensometry

locally and safely up to sample fracture. Comparison with tensile tests on dog bone samples without waist (DIN53504-S2) proved that waisted specimens provide the same curves for $F\left(\lambda_1, \; \dot{\lambda}_1 = \text{const.}\right)$.

For the test, a specimen is clamped inside a customised box (adapted from [38]) where test atmosphere and temperature are under control (according to Table 3). Figure 3 shows the whole set-up.

After equilibration of temperature (fluctuation $<$ 1 K) and humidity under $\sim$1 N pre-load, all experiments are carried out under longitudinal stretch control via extensometry which simultaneously monitors longitudinal stretch, $\lambda_1 = \frac{l}{l_0}$, and transverse stretch, $\lambda_2 = \frac{b}{b_0}$, at the markers at the sample centre (Figs. 2, 3b). A conservative estimate confirms that 15 min. of equilibration is enough to obtain a constant temperature across the specimen. With the measured longitudinal force, $F(t)$, and isotropic deformation of the amorphous sample, the Cauchy stress component, T_{11}, follows from

$$T_{11} = \frac{F}{b \cdot d}, \quad b = d \tag{1}$$

and the Poisson ratio, ν, from

$$\nu = -\left.\frac{d\lambda_2}{d\lambda_1}\right|_{\lambda_1=1}, \quad \lambda_1 = \frac{l}{l_0} \quad \lambda_2 = \frac{b}{b_0} = \lambda_3 = \frac{d}{d_0} \tag{2}$$

For the major part of the measurements, we record $F(t)$, $l(t)$ and $b(t)$ at constant stretch rate, $\dot{\lambda}_1$, of 10^{-3} s^{-1} or 10^{-2} s^{-1}. As the worst case, $\dot{\lambda}_1 =$ const. is reached at $\lambda_1 \approx 1.01$ for $\dot{\lambda}_1 = 10^{-2}$s^{-1}. After acceleration to $\dot{\lambda}_1 =$ const., the deviation from the nominal rate is less than 1%. Two rates help to describe the viscoelastic response at the various measuring temperatures and ageing states.

For each state of ageing, 4–5 specimens are tested at the various T_{test} and $\dot{\lambda}_1$.

Moreover, the stress relaxation, T_{11} (t), of freshly prepared samples is recorded in the viscoelastic state (26 °C ± 0.1 K). A pre-stretch from zero to 1.42 is applied to each specimen. Then, three subsequent λ_1-steps ($\Delta\lambda_1 = +0.06$) are executed with $\dot{\lambda}_1 = 3 \cdot 10^{-3}$s^{-1}. This small stretch rate provides a smooth transition from the step to the plateau of λ_1 without overshooting. For a given λ_1-level, 4 hours is enough to reach the T_{11}-plateau in the limits of experimental noise ($\sim$0.05 MPa) of the force sensor. Via the pre-stretch variation for an ensemble of specimens, the λ_1-range is extended to 42 levels from $\lambda_1 = 1 \ldots 1.54$ with an effective data point distance of $\Delta\lambda_1 = 0.03$.

3 Results and discussion

3.1 Properties of the juvenile polyurethane

The *ATR IR spectrum* (Fig. 4) provides information on the chemical structure of the PU9010 network in the dry state right after preparation.

All major bands characterise an amorphous PU made of the three monomers introduced in Sect. 2.1. The bands serve as reference for the discussion of ageing effects in Sects. 3.3 and 3.4. Traces of residual isocyanate (Fig. 4a, inset for $\nu_a(-N=C=O)$ @ 2270 cm^{-1}) and uretdione (Fig. 4b, inset for $\nu(-C=O)$ @ 1780 cm^{-1}, uretdione groups are a chemical modification made by the manufacturer of the MDI monomer) are at the detection limit. The few isocyanate groups did not find a reaction partner (OH group) as they are mounted by accident at unfavourable positions in the growing network. Urea is not detected. Hence, the preparation in dried air avoided the unwanted side reaction of isocyanate with water. Additional tests proved both the reproducibility of sample preparation and chemical stability during storage under dried air.

Figure 5 shows an example for *DSC curves of freshly prepared PU9010* according to the protocol in Sect. 2.4.1, and the first derivative of the specific heat flow, ϕ, with respect to temperature, T.

The heat flow step indicating the caloric glass transition (GT$^{\text{cal}}$) is the only feature in the curves. There is no indication of first-order phase transitions in the juvenile PU9010. This finding meets the expectation from the structure of the monomers—the resulting PU network is amorphous. For the first heating run with the juvenile sample, an enthalpic peak (at $\sim$38 °C) indicates clearly a retarded release of some thermal degrees of freedom at the upper end of GT$^{\text{cal}}$. Such enthalpy retardation evidences some local non-equilibrium structure of hindered mobility developed in the amorphous network during chemical formation. It relaxes with the first heating as no enthalpy retardation occurs in the subsequent runs. In turn, the GT$^{\text{cal}}$ of the dry, thermally relaxed network is obtained in the second and third heating runs. The two curves coincide, and this documents a stable state without thermal destruction. The first derivative of ϕ is most suitable to read the parameters of GT$^{\text{cal}}$: the caloric glass transition temperature, T_g^{cal}, the low and the high end at $T_{\text{GT start}}^{\text{cal}}$ and $T_{\text{GT end}}^{\text{cal}}$, respectively.

With that, the width, ΔT_g^{cal},

$$\Delta T_g^{\text{cal}} = T_{\text{GT end}}^{\text{cal}} - T_{\text{GT start}}^{\text{cal}} \tag{3}$$

the skewness, skwT_g^{cal},

$$\text{skw}T_g^{\text{cal}} = \frac{T_g^{\text{cal}} - T_{\text{GT start}}^{\text{cal}}}{T_{\text{GT end}}^{\text{cal}} - T_g^{\text{cal}}} \tag{4}$$

and the step height, Δc_p^{GT}, of the specific heat capacity, c_p

$$\Delta c_p^{\text{GT}} = c_p \left(T_{\text{GT end}}^{\text{cal}} \right) - c_p \left(T_{\text{GT start}}^{\text{cal}} \right) \tag{5}$$

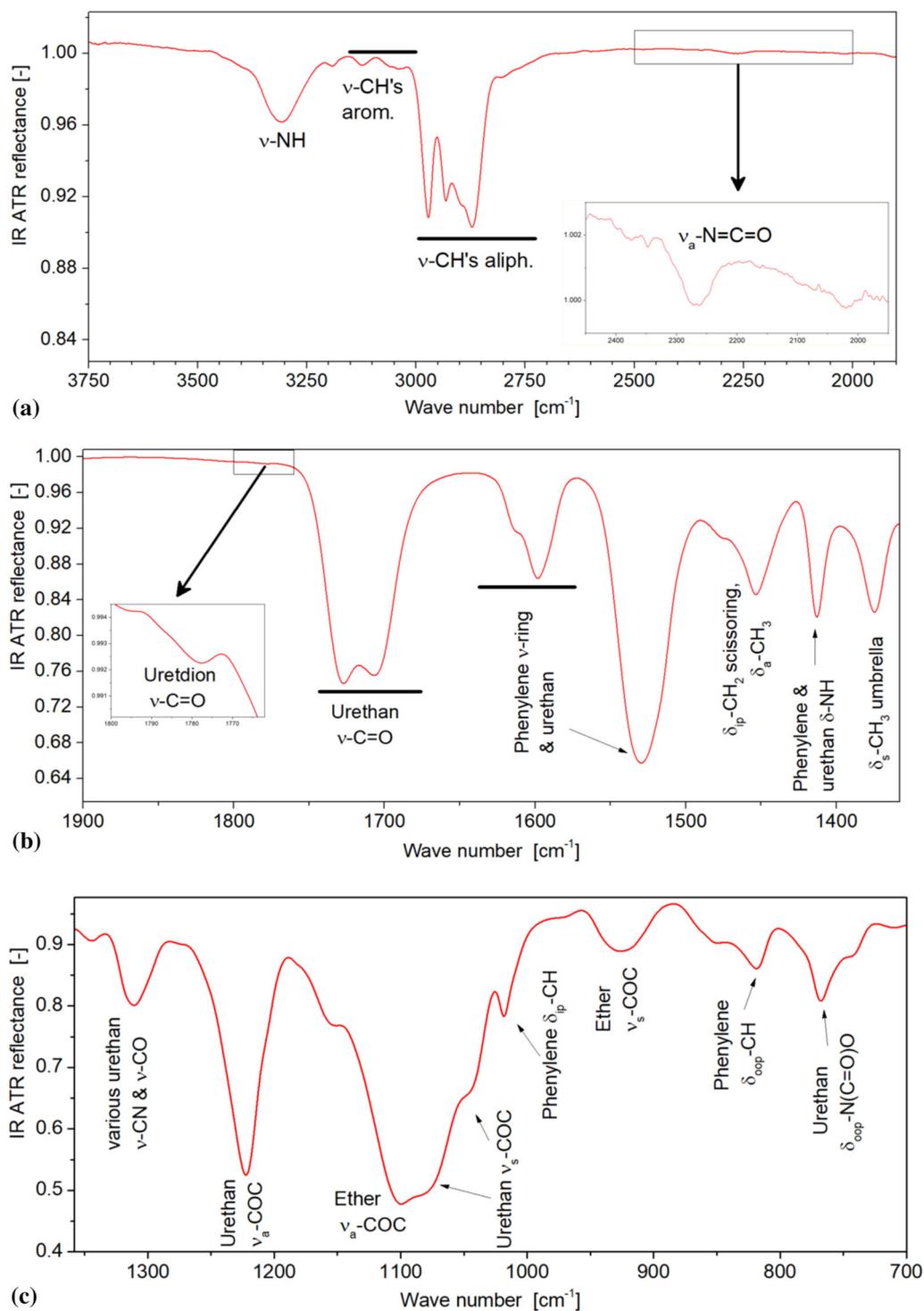are defined as additional features of the caloric glass transition.

Fig. 4 As-prepared dry PU9010. The ATR IR spectrum (adapted from [30]) with band assignment according to [40,41]
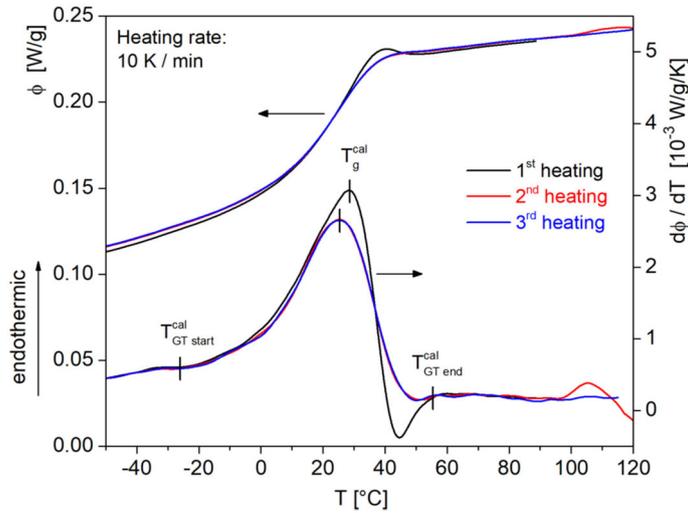
Fig. 5 Specific heat flow, ϕ (T), and its first derivative as measured by DSC for three subsequent heating runs for juvenile PU9010 (adapted from [30])

From 16 batches of juvenile PU9010, we get $T_{GT\,start}^{cal} = -26.7\,°C \pm 4.7$ K, $T_g^{cal} = 25.8\,°C \pm 0.7$ K, $T_{GT\,end}^{cal} = 51.7\,°C \pm 1.7$ K, and $\Delta c_p^{GT} = (440 \pm 30)$ mJ $\cdot$ g^{-1} $\cdot$ K^{-1} from the third heating run. The small errors illustrate very good reproducibility. Only $T_{GT\,start}^{cal}$ possesses a larger scatter because this temperature is hard to determine in view of the long tail of GT^{cal} at low temperature. The remarkable width $\Delta T_g^{cal} \approx 78$ K and skewness skw$T_g^{cal} \approx 2$ of GT^{cal} indicate a wide spectrum of thermal degrees of freedom that become active while heating through the glass transition. Storage in dried air for up to 28 days has no effect either.

We note in passing that the caloric data depend on the T-rate chosen in the DSC experiment. In that sense, GT^{cal} depicts the *dynamic* response of the degrees of freedom of the polymer to changing temperature.

Tensile tests elucidate the mechanical properties of the juvenile PU9010 as a reference for the aged states. Stress relaxation experiments at 26 °C (experimental schedule see Sect. 2.4.2) map the linear viscoelastic behaviour because $T_{test} = T_g^{cal}$. Figure 6 provides two examples of the measured relaxation curves, T_{11} (t, $\lambda_1 =$ const., $T_{test} = 26$ °C), and for the Wiechert model fitted with five relaxation times, $\tau_i = 1,\ 10,\ 10^2,\ 10^3,$ and 10^4 s, according to

$$T_{11}^{relax}(t \geq t_1, \lambda_1 = const.) = E_{relax} \cdot \dot{\lambda}_1 \cdot t_1 + \sum_{i=1}^{5} E_i \cdot \tau_i \cdot r \cdot \left(\exp\left(-\frac{(t - t_1)}{\tau_i} \right) - \exp\left(-\frac{t}{\tau_i} \right) \right) \quad (6)$$
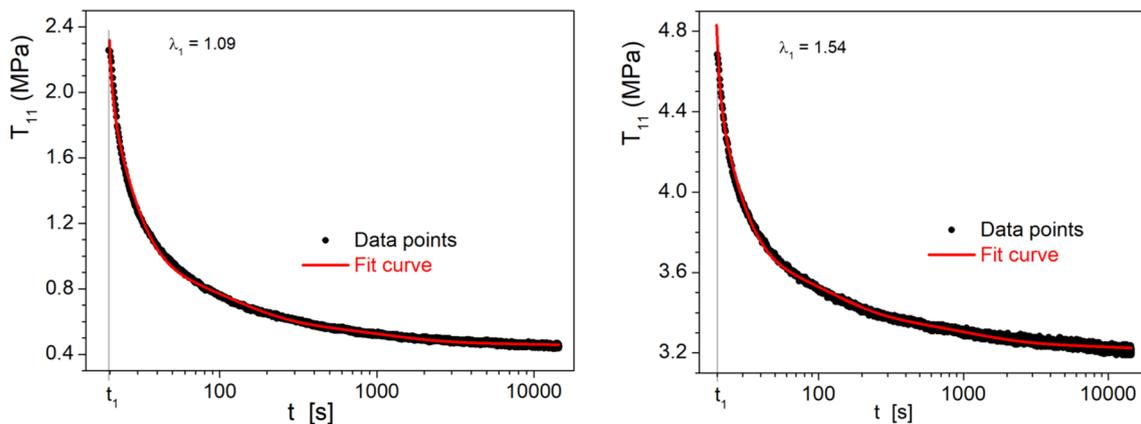

Fig. 6 Juvenile PU9010—two stress relaxations at 26 °C. Raw data from [42], plots adapted from [30]

with E_{relax} = tensile modulus of the relaxed elastic response,

$\dot{\lambda}_1$ = const. = stretch rate during the $\Delta\lambda_1$-step to approach the selected level of λ_1=const., t_1 = start of stress relaxation at the selected level of λ_1 = const., as obtained from Fig. 6.

E_i = moduli of the springs in the five Maxwell elements of the Wiechert model.

The fitting of Eq. (6) to the measured force relaxation curves, T_{11} (t), is done with the software OriginPro. For a fit, the E_{relax} value is taken from the measured plateau value, $T_{11}(t)$ = const., by

$$E_{relax} =: \frac{T_{11} (t) = const.}{(\lambda_1 - 1) = const.} \tag{7}$$

For $\lambda_1 \leq 1.27$, E_{relax} (26 °C) = (5.15 ± 0.34) MPa is constant. For λ_1 beyond 1.27, E_{relax} slightly rises to ≈ 6 MPa at $\lambda_1 = 1.54$ indicating the transition to nonlinear deformation due to the beginning orientation and packing of network chains.

Figure 7 provides the resulting relaxation time spectra, $H(\tau_i)$, with the discrete relaxator strengths for $\tau_i = 1, 10, 10^2, 10^3, 10^4$ s according to

$$H(\tau_i) \approx \tau_i \cdot \sum_{j=1}^{5} \frac{E_j}{\tau_j} \cdot \exp\left(-\frac{\tau_j}{\tau_i}\right) \tag{8}$$

Within scatter, the relaxation time spectra do not depend on the stretch for $\lambda_1 \leq 1.27$. For larger stretch levels, the relaxator strength, $H(\tau_1 = 1$ s), for the shortest relaxation time tends to decrease, while the relaxator strengths for the large relaxation times τ_4, τ_5 tend to increase (Fig. 7, blue arrows). These trends show that the cooperative mobility of network chains is affected when the material deforms beyond the linear response—as seen for the relaxed modulus, E_{relax}.

In the *isothermal tensile tests* with $\dot{\lambda}_1$ = const., the mechanical properties can be determined for stretches before material damage starts. Corresponding measurements for the worst choice of $\dot{\lambda}_1$ and T_{test} prove the absence of damage for $\lambda_1^{max} \leq 1.35$.

The Poisson's ratio, ν, is important for a proper choice of the mechanical material law. Figure 8 shows the data calculated with Eq. (2) from the measurement of λ_1 and λ_2 during stressing the relaxation experiments and the tensile tests at λ_1 = const..

Note that $\nu \approx 0.5$ (incompressibility) is observed for the *relaxed* PU9010 with the stress relaxation experiments. The effects of $\dot{\lambda}_1$ and T_{test} are small and the experimental scatter is quite big, but in tensile testing, the *dynamic* ν tends to decline with decreasing T_{test} and rising $\dot{\lambda}_1$. In addition, the sample volume declines for $\lambda_1 > 1.25$ (data not shown here). Other studies [43–45] report similar effects for polymer networks. Therefore, compressibility shall be taken into account and hence we use the neo-Hooke law for isotropic compressible
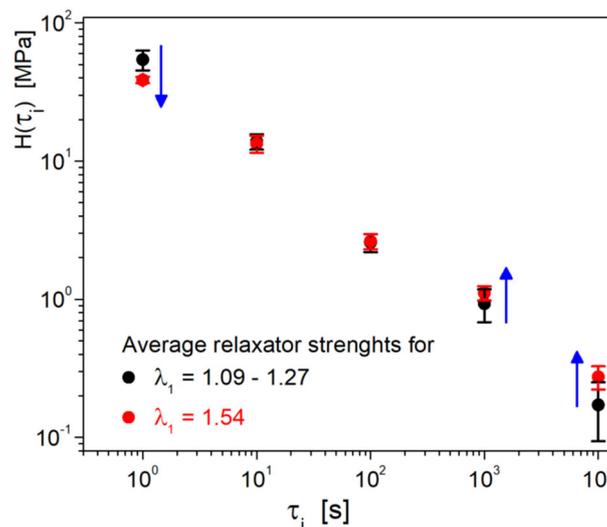

Fig. 7 Discrete relaxation time spectra for $\lambda_1 = 1.09 - 1.27$ and for $\lambda_1 = 1.54$ (raw data from [42], plots adapted from [30])
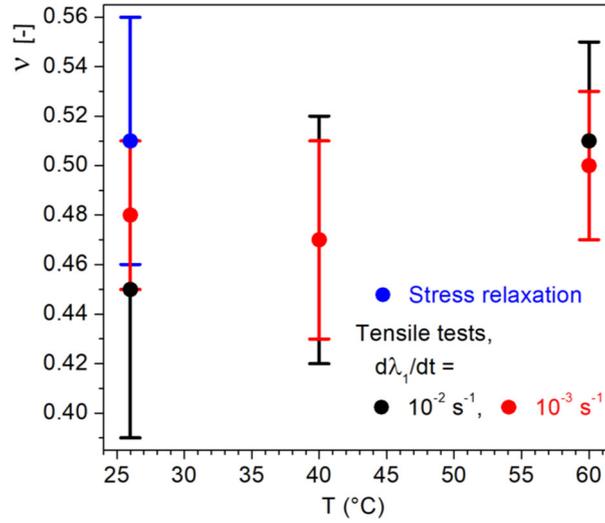
Fig. 8 Poisson's ratio, ν, as a function of the test temperature, T_{test}, for $\lambda_1 < 1.25$ (raw data from [39], plot adapted from [30])

media, here for uniaxial tension

$$T_{11}(\lambda_1, \lambda_2, T_{\text{test}} = \text{const.}) = \mu(T_{\text{test}}) \cdot \frac{\lambda_1^2 - \lambda_2^2}{\lambda_1 \cdot \lambda_2^2} \tag{9}$$

$\mu =$ shear modulus,
as material law for PU9010. Furthermore, Young's modulus, E, can be determined by

$$E =: \left. \frac{dT_{11}}{d\lambda_1} \right|_{\lambda_1=1,\ \lambda_2=1} \overset{\text{eqs.(9, 2)}}{=} 2(1+\nu)\mu \tag{10}$$

The experimental results for $T_{11}(\lambda_1, \dot{\lambda}_1 = \text{const.}, T_{\text{test}} = \text{const.})$ confirm the chosen material law—cf. Fig. 9 for an example for isothermal tensile tests with variations of T_{test} and $\dot{\lambda}_1$. The Neo-Hookean deformation measure, $\frac{\lambda_1^2 - \lambda_2^2}{\lambda_1 \cdot \lambda_2^2}$, ranges up to only 1.45 (i.e. $\lambda_1 = 1.42\ldots1.45$, depending on T_{test}) because the T_{11}-data bend upwards for larger values due to beginning orientation and packing of network chains.

At $T_{\text{test}} = 26\,°C$, the T_{11}-curves strongly bend in the *initial* stretch range for both deformation rates. The viscoelastic sample is in the dynamic glass transition, and hence it needs some time to arrive in the steady regime of deformation. This non-steady stage diminishes quickly with increasing temperature. At 40 °C, the
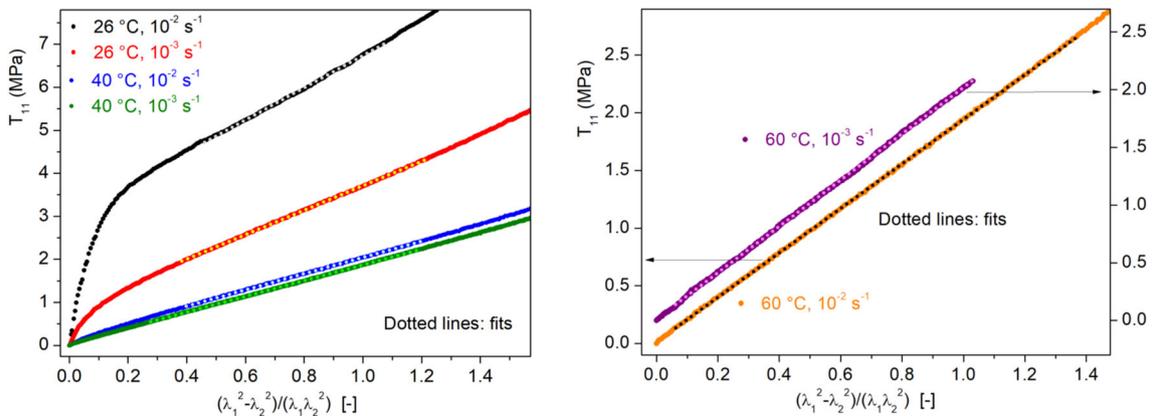

Fig. 9 Tensile tests of juvenile PU9010—neo-Hooke plot for the true stress, T_{11} (raw data from [39], plots adapted from [30]). Linear range of the T_{11}-curves is fitted by Eq. (9)—dotted lines
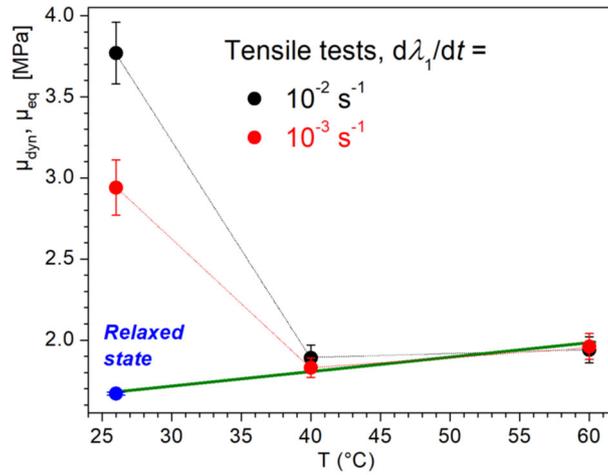
Fig. 10 Shear moduli of juvenile PU9010 (raw data from [39], plot adapted from [30]). Dotted lines as guide for the eye. Green solid line—linear regression (colour figure online)

curvature is adumbrated only for $\dot{\lambda}_1 = 10^{-2}$ s^{-1}, but the slope in the linear range still depends on $\dot{\lambda}_1$. Neither the curvature nor the rate dependence is found at 60 °C anymore because the sample has become rubber-like. Interestingly, the PU9010 obeys the compressible isotropic neo-Hooke's law for steady deformation under any condition of T_{test} and $\dot{\lambda}_1$, including viscoelastic response. Hence, a shear modulus can be determined for the neo-Hooke deformation range, i.e. the linear segments in Fig. 9, but we have to distinguish the *dynamic* shear modulus, $\mu_{dyn} (\dot{\lambda}_1, T_{test})$, for viscoelastic response in the dynamic glass transition from the *equilibrium* modulus, $\mu_{eq} (T_{test})$, for the rubbery state. Figure 10 summarises the shear modulus data for juvenile PU9010.

The $\dot{\lambda}_1$-dependence of μ_{dyn} is obvious for T_{test} within GT^{cal} (at 26 °C and still at 40 °C), whereas it disappeared at 60 °C in the rubbery state.

For the shear modulus in the entropy elastic state of amorphous isotropic polymer networks, polymer physics provides linear equations like

$$\mu \left(T^{abs}\right) = Q \cdot T^{abs}, \quad Q = \text{const.}, \quad T^{abs} - \text{absolute temperature [K]} \tag{11}$$

The constant, Q, relates inversely to some 'effective' average molar mass of the network chains, i.e. Q is proportional to the 'effective' cross-link density. Now, linear regression with Eq. (11) provides an interesting result: The values for the relaxed shear modulus, μ_{relax} (from Eq. (10) with E$_{relax}$ from the stress relaxation experiment) and for the μ_{dyn}-data measured at $\dot{\lambda}_1 = 10^{-3}$ s^{-1} for 40 °C and 60 °C meet the straight line very well (green line, Fig. 10). Three conclusions follow: (i) these μ_{dyn}-data represent the relaxed mechanical state for the corresponding temperatures, (ii) μ_{relax} and the two μ_{dyn}-data result from the configurational entropy contribution to the stiffness of PU9010, including the glass transition, and (iii) the slope of the straight line gives a measure of the 'effective' cross-link density in the network. This 'effective' cross-link density comprises the average density of chemical cross-links and some structural obstructions like dead chain ends or residual monomers/oligomers without chemical link to the network.

3.2 Water uptake kinetics and desorption

Figure 11 shows the gravimetric water uptake of initially dry PU9010 specimens during the first 3 weeks of exposure time, t, to air of various levels of humidity. The water uptake is given by the relative mass change, Δm_{rel}, according to

$$\Delta m_{rel} (t) = \frac{m_{\text{exposed sample}} (t) - m_{\text{dry sample}}}{m_{\text{dry sample}}} \cdot 100 \tag{12}$$
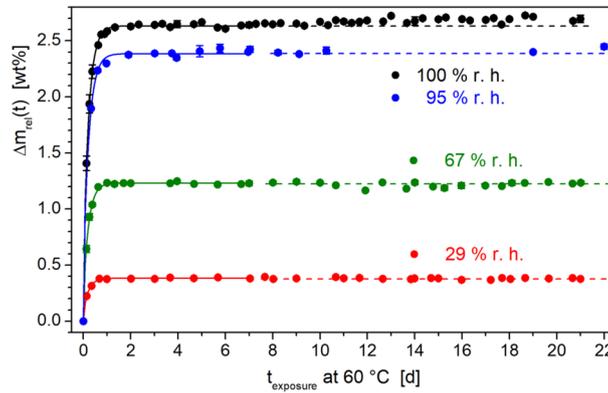
Fig. 11 Relative mass change, Δm_{rel}, (in wt%) of juvenile PU9010 during storage at 60 °C in air of various humidity levels. Mostly, the error bars are smaller than the data point size. Raw data for 100% r. h. from [39], plot adapted from [30]. Solid curves represent the fits according to Fickian diffusion for $t \leq 7$ d—Eq. (13). Dashed lines—extrapolation of the fitted plateau value from $c_{H_2O, \infty}$(r.h)

Table 4 PU9010 water uptake at 60 °C for up to 1 week in air of various humidity—Fickian diffusion parameters according to Eq. (13)

r. h. of surrounding air (%)	H$_2$O content in surrounding air [g$_{H_2O}$/kg$_{air}$]	Sample			r^2
		d_P [mm]	D_{Fick} [m^2/s]	$c_{H_2O, \infty}$ [wt%]	
29	38	1.95 ± 0.04	$(2.09 \pm 0.09) \cdot 10^{-11}$	0.384 ± 0.002	1.00
67	94	2.00 ± 0.07	$(2.14 \pm 0.05) \cdot 10^{-11}$	1.232 ± 0.004	1.00
95	143	2.00 ± 0.07	$(1.98 \pm 0.08) \cdot 10^{-11}$	2.385 ± 0.010	1.00
100	152	2.01 ± 0.11	$(2.08 \pm 0.03) \cdot 10^{-11}$	2.632 ± 0.005	1.00

The thin specimens (see Table 4 for d_P) need less than a day to establish a constant water content. That plateau relates to the humidity in the surrounding air. For the first 7 d, Fickian diffusion describes the water uptake kinetics very well as shown in Fig. 11 by the solid curves fitted by

$$c_{H_2O}(t) = \frac{m_{H_2O}(t)}{m_{dry\ plate}} = c_{H_2O, \infty} \left(1 - \frac{8}{\pi^2} \sum_{n=0}^{\infty} \frac{1}{(2n+1)^2} \exp\left(-D_{Fick} \cdot (2n+1)^2 \cdot \pi^2 \cdot \frac{t}{d_P^2} \right) \right) \quad (13)$$

$c_{H_2O}(t)$ = mass concentration of H$_2$O in the plate at exposure time t,

$m_{H_2O}(t)$ = mass of water in the plate at t,

$c_{H_2O,\infty} = \lim_{t \to \infty} c_{H_2O}(t)$ = water equilibrium concentration inside the plate (plateau value),

D_{Fick} = const. = diffusion coefficient,

which is Fick's model for one-dimensional diffusion in a plate of thickness, d_P, at constant temperature [46]. The fitting of Eq. (13) to the measured water uptake curves is done with the software OriginPro. The specimens are thick enough to neglect re-drying during weighing. Table 4 summarises the fit results.

The coefficient of diffusion does not depend on humidity (average value D_{Fick} (60 °C) = $(2.1 \pm 0.1) \cdot 10^{-11}$ m^2 s^{-1}), but the plateau concentration, $c_{H_2O, \infty}$(r. h.), increases due to the rising chemical potential of water in the surrounding humid air.

Moreover, according to the model of regular solutions (e.g. [47,48]), the upward bending of the trend curve in Fig. 12 indicates *endothermic* mixing of water with PU9010. Hence, with increasing water content, the interaction between H$_2$O molecules tends to exceed the H$_2$O–PU interaction (cf. the model of regular solutions, the GAB model by Guggenheim, Anderson and de Boer [49–52] or the cluster model by Zimm and Lundberg [49,53]).

As the consequence, the H$_2$O molecules tend to cluster with increasing concentration in PU9010. Figure 13 provides a first proof for this conclusion.

The PU keeps the water content plateau at 95% r. h. on the long term, and the samples remain transparent. Only for exposure to 100% r. h., an additional water uptake of ~0.05 wt% (Fig. 13—green arrow) starts at
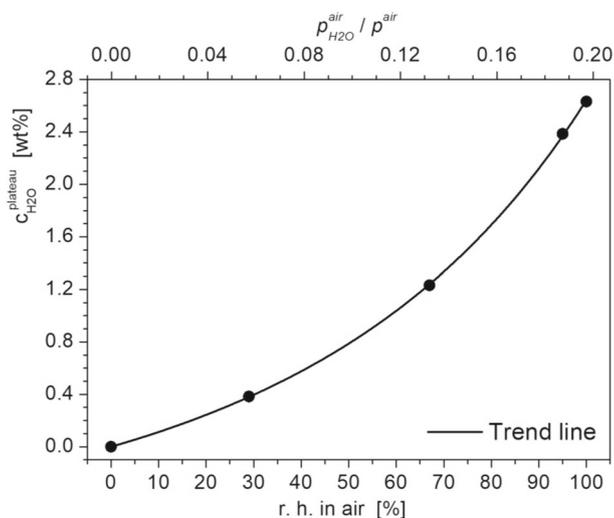
Fig. 12 Water equilibrium concentration, $c_{H_2O}^{plateau} = c_{H_2O,\infty}$, in PU9010 at 60 °C as a function of relative humidity or normalised partial water vapour pressure, $p_{H_2O}^{air}/p^{air}$, in the surrounding air. Solid line—guide to the eye. Plot adapted from [30]
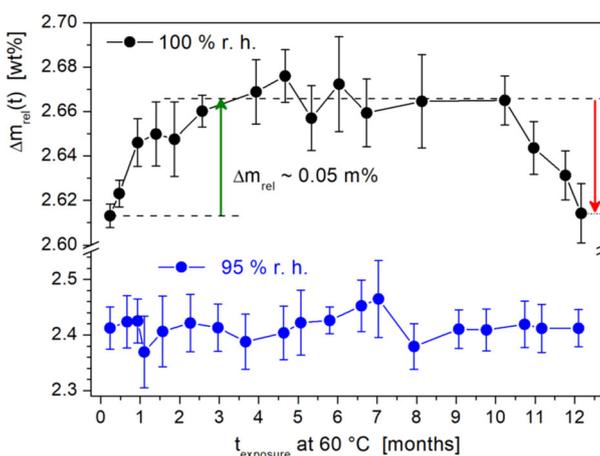

Fig. 13 Evolution of the relative mass change, Δm_{rel}, in PU9010 during long-term storage (7 d–12 months) at 60°C in humid air (95 and 100% r. h., respectively). Plot adapted from [30]

$t_{exposure} \approx 10$ h and completes within 4–5 months. That uptake goes with an evolution of sample opacity. The opacity vanishes by sample re-drying at 60 °C. Therefore, we attribute these effects to finely dispersed, H_2O-rich regions in the PU. More insight into the mechanism follows in Sects. 3.4.2 and 3.4.3.

Finally, for all levels of humidity, the samples recover their initial mass after up to 3 weeks of re-drying at room temperature. Hence, Δm_{rel} is due only to water uptake on the short term.

However, after 10 months of exposure and only at 100% r. h., the sample mass decreases by roughly 0.05 wt% (Fig. 13—red arrow). Re-drying of these samples after 12 months of exposure verifies the reason. The samples lost $\sim$0.05 wt% of their initial mass. In air with $\leq$95% r. h., no weight loss is found during long-term exposure. In conclusion, a high water content forces products of chemical degradation (i.e. network chain cleavage at urethane groups [6]) to desorb slowly from PU9010 during prolonged ageing at 60 °C.

3.3 Chemical ageing effects in moist–warm air

In this study, the term 'chemical ageing' embraces all chemical changes that proceed in the polymer under the influence of external stimuli—here temperature and humid air. Chemical ageing is studied by IR ATR spectroscopy. Neither the water content in the specimen nor prolonged ageing significantly affect the band for
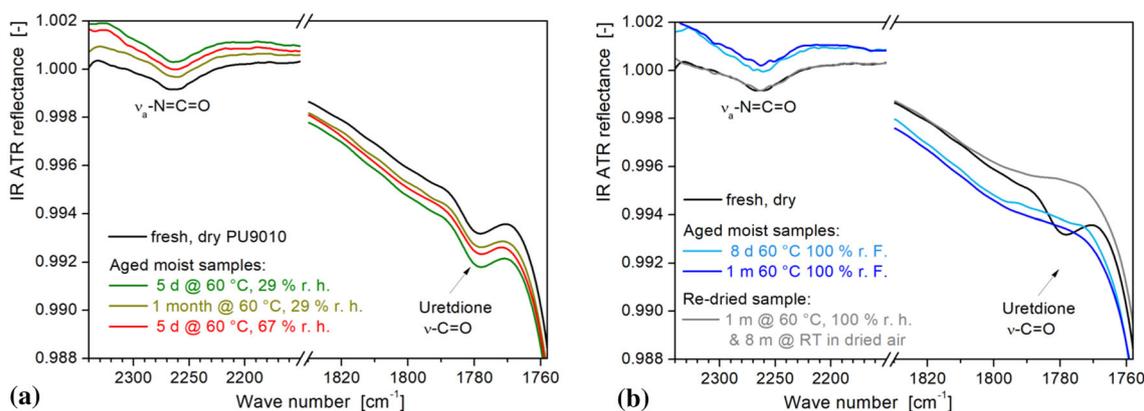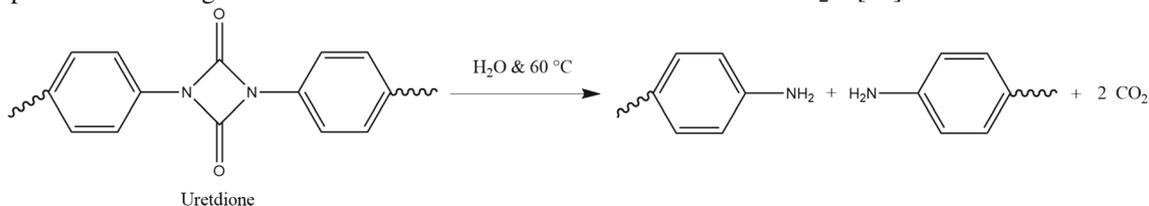
Fig. 14 Spectral regions of the isocyanate and uretdione stretch vibrations for PU9010, after ageing. **a** Ageing at 60 °C, 29 or 67% r. h. **b** Ageing at 60 °C, 100% r. h. and the PU after 8 months of re-drying in dried air at room temperature. Plots adapted from [30]

the $\delta_s - CH_3$ umbrella vibration mode (~ 1374 cm^{-1}). Therefore, the spectra are normalised to the intensity of this band in order to attain comparability.

Upon short-term ageing, the major bands do not show permanent spectral changes in water-saturated PU9010. The uretdione band provides the only exception—Fig. 14.

For low humidity of 29 or 67% r. h. in the surrounding air, the small band (~ 1780 cm^{-1}) for uretdione groups does not change. Only for the highest water content (100% r. h.), the band vanishes quickly with exposure. The fading band indicates a chemical reaction of uretdione with H_2O [54].

The result is a permanent cleavage of network chains. Owing to the very low uretdione content in PU9010, significantly changed material properties of the PU network are not expected, however. Surprisingly, H_2O does not attack the residual isocyanate groups at all. As Fig. 14a, b show, the isocyanate band (ν_a-N = C = O at 2270 cm^{-1}) does not change at any level of moisture during one month of ageing, and after 8 months of gentle re-drying at room temperature, it coincides with the band found for the juvenile PU9010. Therefore, the surrounding network screens those residual isocyanate groups very well from the H_2O molecules.

For long-term exposure to 100% r. h. air at 60 °C, re-dried PU9010 sheets are studied in order to elucidate permanent chemical modifications. Figure 15 compares the normalised spectrum of juvenile samples with those recorded on re-dried samples after 2 and 11 months of ageing.

After 11 months in 100% moist air, almost all spectral regions of the *re-dried* PU9010 coincide with the juvenile state. This result documents the excellent chemical stability of the PU. Permanent changes arise only in two narrow regions—cf. the red boxes in Fig. 15b, c. These changes cannot be assigned to specific vibrations. Possibly, they depict delocalised vibrations, which are sensitive to changes of the packing of the network chains due to water uptake and desorption.

In conclusion, the PU9010 undergoes minor chemical changes even during 11 months of hygro-thermal ageing. This finding corresponds to the very small mass loss of 0.05% described in Sect. 3.2 for long-term exposure, and it agrees with the superb stability reported in the literature for poly(ether urethanes) (e.g. [55]).

3.4 Physical ageing effects in moist–warm air

It should be noted that physical ageing includes all property changes that come without a change of the *chemical* structure of the material. That statement sounds a bit different from definitions in the literature where physical ageing is commonly understood as *'reversible'* change of material properties. Reversibility is a problematic
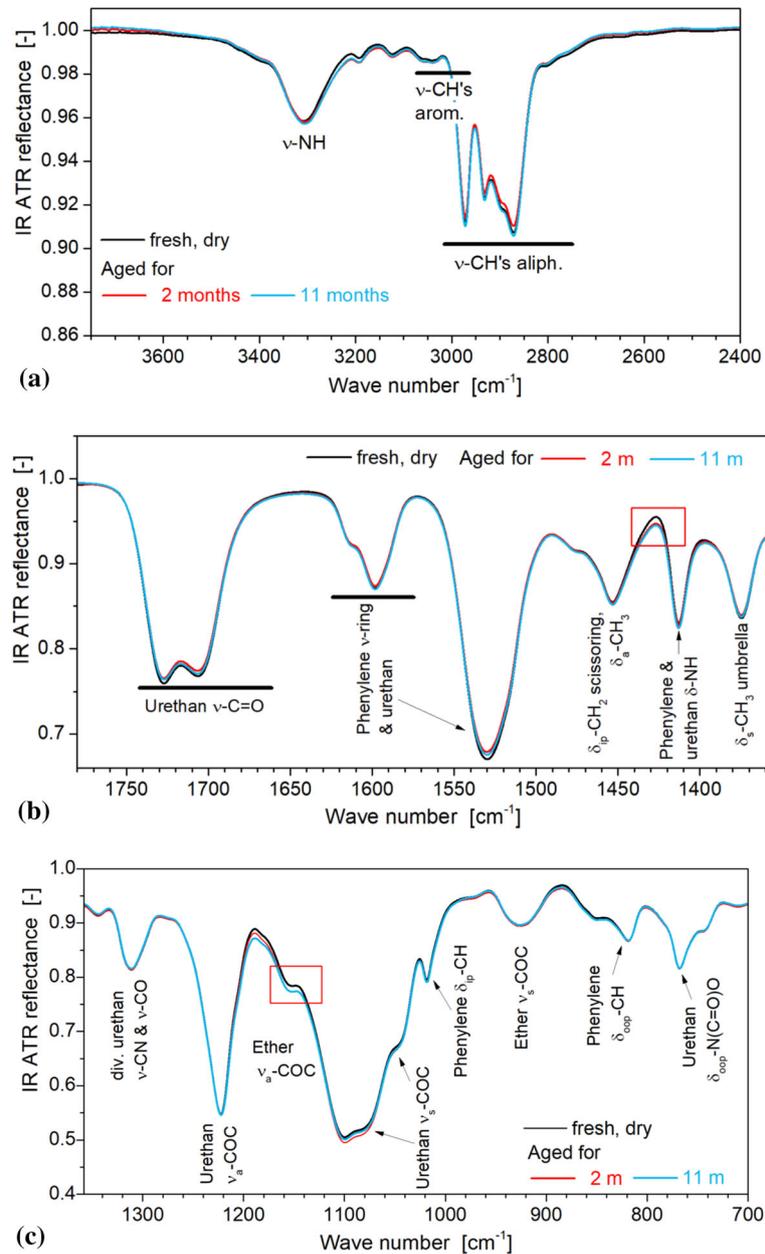
Fig. 15 Normalised IR ATR spectra for juvenile PU9010 versus specimens re-dried (1 month at room temperature) after ageing in humid air for 2 and 11 months, respectively. Red boxes—spectral regions with permanent changes. Plots adapted from [30]

term in the context of polymer ageing, however, because very often *the polymer state prior to and/or after ageing* is characterised by durable non-equilibria with respect to structure and mobility. Such non-equilibria will not restore spontaneously after the ageing conditions were reset to the initial environmental conditions. Hence, we have to consider changes of non-equilibria, and these changes take place by thermodynamically 'irreversible' processes. The resulting 'irreversibility' is the result of *physical* ageing. Thus, physical ageing must not be considered as a reversible process.

3.4.1 Short-term ageing and evolution of the caloric glass transition

Figure 16 displays the DSC results for fully water-saturated samples after a few days of exposure.
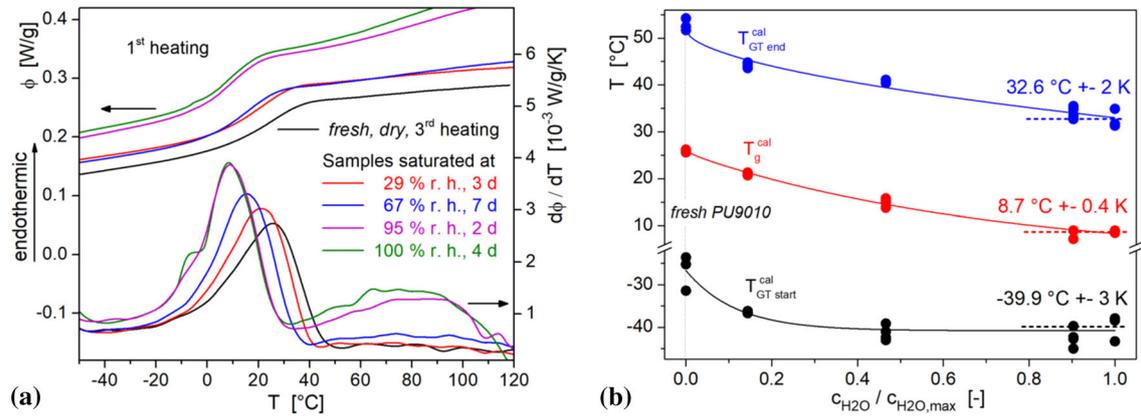Above GT^{cal}, a broad endothermic peak documents the temperature-driven desorption of water.

Fig. 16 First heating in DSC for saturated PU9010 aged at 60 °C in humid air, and third heating of juvenile material for reference. Plots adapted from [30]. **a** Specific heat flow, $\phi(T)$, and its first derivative. **b** Parameters of GT^{cal} as a function of water content, c_{H2O}, in the samples, normalised to the maximum water concentration, $c_{H2O,max}$, obtained in 100% r. h. (cf. Table 4). Solid lines as guide to the eye
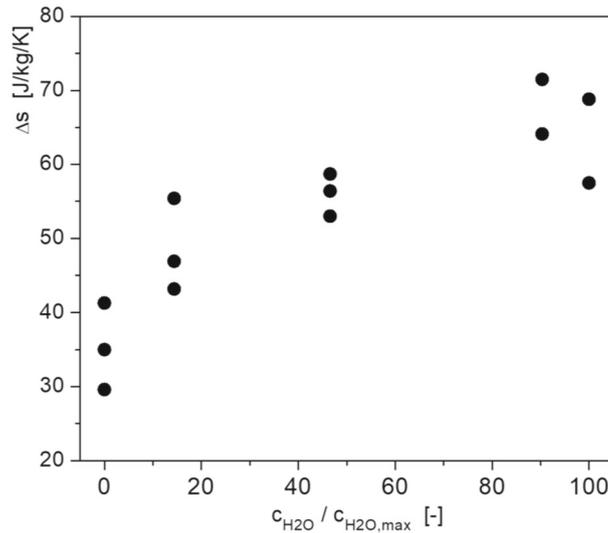

Fig. 17 Specific entropy gain, Δs, across GT^{cal} as a function of the normalised water concentration in PU9010 saturated at 60 °C in humid air (0, 29, 67, 95 or 100% r. h.). Plot adapted from [30]

For 100% r. h., the $\phi(T)$-curve shows a weak shoulder at about -6 °C. This feature will be discussed in detail in Sect. 3.4.3.

Concerning GT^{cal} (Fig. 16a), first the enthalpy retardation at the upper end of GT^{cal} (cf. Fig. 5) disappeared during short-term ageing. Second, with increasing water content in saturated PU9010, GT^{cal} shifts downwards to $T_g^{cal} \approx 8.7$ °C ± 0.4 K for $c_{H_2O} = c_{H2O,max}$ (Fig. 16b), while the width, $\Delta T_g^{cal} \approx 76.5$ K, and the skewness, $skwT_g^{cal} \approx 2$, do not change with respect to the juvenile PU (cf. Sect. 3.1). These findings attest that water in the polymer network relaxes the regions of initially hampered mobility and facilitates the whole spectrum of thermal degrees of freedom in the polymer. Third, with the well-known thermodynamic equation for a specific entropy change, the measured $\phi(T)$ provides the specific entropy gain, Δs

$$\Delta s = \int_{-40\,°C}^{50\,°C} \frac{c_p(T)}{T}\,dT = \int_{-40\,°C}^{50\,°C} \frac{\phi(T)}{\dot{T}\cdot T}\,dT, \tag{14}$$
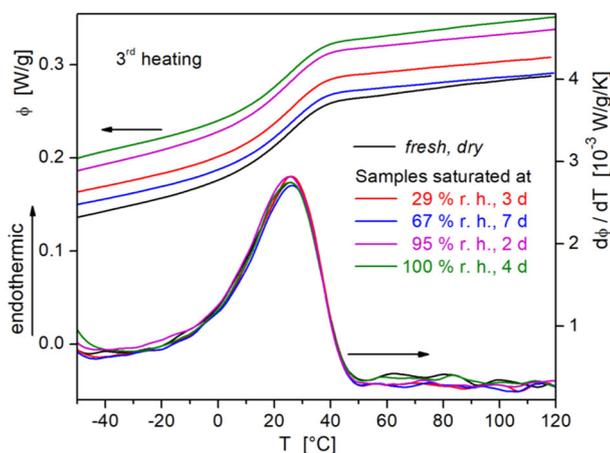
across GT^{cal}—Fig. 17.

Fig. 18 Specific heat flow, $\phi(T)$, and its first derivative as measured in the third DSC heating run for saturated PU9010 aged at 60 °C in air of denoted humidity and for the juvenile material. Plot adapted from [30]
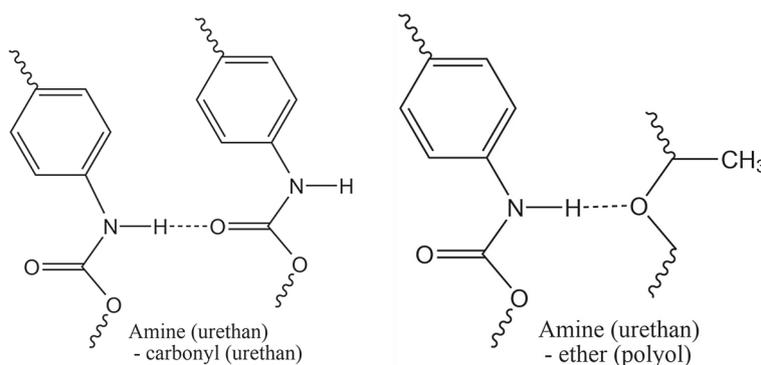

Fig. 19 Hydrogen bond types in poly(ether urethanes)

For $c_{H2O} = c_{H2O,max}$, the presence of water roughly doubles Δs as compared to the dry network and thereby the number density of conformational degrees of freedom that 'unfreeze' across GT^{cal}.

In addition, Figs. 16 and 17 reveal that the major changes of the caloric properties are complete with $c_{H2O} \approx 0.4 - 0.5 \, c_{H2O,max}$. Hence, only such part of the H_2O molecules dominates gain and facilitation of the conformational degrees of freedom that go with GT^{cal}. Interestingly, additional DSC heating runs with these samples override all these changes—GT^{cal} of the juvenile PU is restored (Fig. 18).

That finding proves that the minor chemical changes documented in Sect. 3.3 do not affect the GT^{cal} of PU9010 in a measurable way during short-term ageing (up to ∼1 month). Hence, in the first place H_2O only physically promotes the thermal degrees of freedom of the network (cf. Sect 3.4.2). Water will facilitate the mechanical response of PU9010 as well—see Sect. 3.5.

3.4.2 Hydrogen bond exchange

In poly(ether urethanes), hydrogen bonds ('H-bonds') between urethane groups or between urethane and ether groups are an intrinsic mode of interaction between network chains [5,14,15,23,54,56–74]—Fig. 19.

Due to steric and conformational constraints, only part of these functional groups form such H-bonds, but they are crucial for the molecular mobility in the network. Frequently, the IR band at 1765–1650 cm^{-1} for the carbonyl vibration in the urethane group is analysed to get an idea about the H-bond situation in a PU network. Such analyses distinguish between 'non-bonded', 'weakly H-bonded' and 'strongly H-bonded' urethane groups. Otherwise, H_2O molecules are known for their very strong ability to form intermolecular H-bonds.
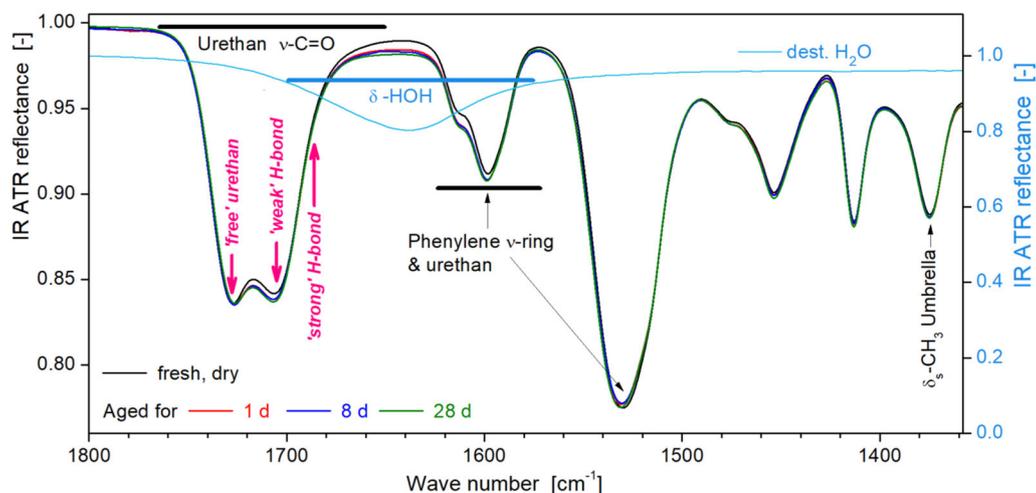
Fig. 20 Normalised IR ATR spectra of PU9010 (left axis): The juvenile sample versus water-saturated specimens after 1, 7 and 28 d exposure to saturated air at 60 °C. The spectra are superposed by vertical shift for better comparison. Red arrows mark the positions of the carbonyl vibration ($\nu - C{=}O$) for non-bonded ('free'), weakly H-bonded and strongly H-bonded urethane groups, respectively (see [30] for more detail). The room temperature spectrum of distilled water is given for information (right axis). Plot adapted from [30]
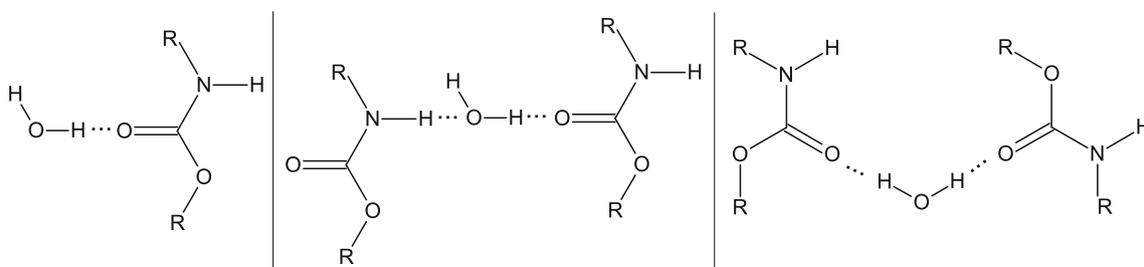

Fig. 21 Model conceptions on H-bonds between H_2O molecules and urethane groups according to [5,23]. Graphics from [30]

Therefore, we reconsider the normalised IR ATR spectra of water-saturated PU9010 sheets with respect to changes of the urethane bands. Figure 20 compares the corresponding spectral region for juvenile PU9010 with water-saturated specimens for a sequence of short ageing times in saturated air.

With its wide δ-HOH band, water in the PU network apparently increases the intensity of the bands for 'weakly' and 'strongly' H-bonded urethane groups, for the 'phenylene ring and urethane' band (1637–1572 cm^{-1}), and for the background in between. These intensity changes evolve within 1 day of exposure, i.e. they complete during the first stage of water uptake and are stable for up to 11 months of ageing. A detailed analysis of the urethane ν-C $=$ O band (subtraction of the δ-HOH band according to water concentration and fit by three Gauss peaks for non-bonded, weakly H-bonded and strongly H-bonded urethane, respectively) reveals the following: (i) the concentration of strong H-bonds does not alter; (ii) the concentration of weak H-bonds grows at the cost of the non-bonded urethanes (see [30] for more detail). The major part of the non-bonded urethane is *not* involved, however. Interestingly, again a water concentration of $c_{H2O} \approx (0.4 \dots 0.5) \cdot c_{H2O,max}$ is sufficient to complete that transformation—as it is the case for maximum gain and facilitation of the thermal degrees of freedom that go with GT^{cal} (see Sect. 3.4.1). Therefore, we conclude that part of the H_2O molecules replace weak H-bonds between urethane groups and form supplementary weak H-bonds with some of the originally non-bonded urethane groups. These mechanisms facilitate the cooperative mobility of the PU network chains.

In the literature, IR studies on H-bonds between H_2O and urethane groups are rare [5,23], but they also observe a rising concentration of H-bonded carbonyls in urethane groups due to water uptake. Figure 21 illustrates the corresponding model conceptions that agree very well with our results.

Note there is no well-founded assignment of these models to the IR band components introduced above.
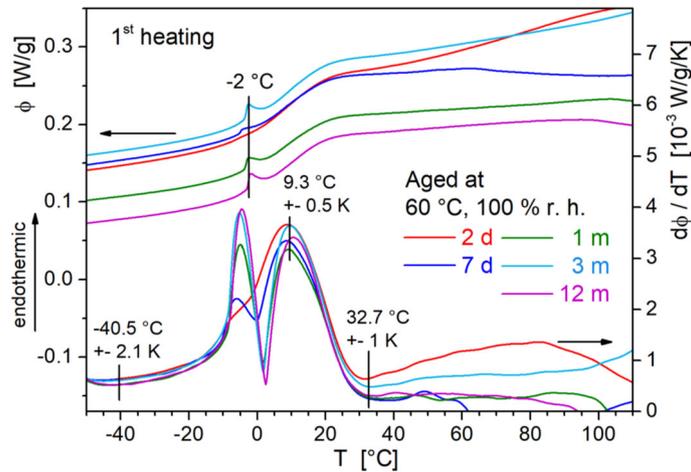
Fig. 22 Selected DSC curves for the first heating of saturated PU9010 specimens during long-term exposure to water-saturated air (100% r. h.) at 60 °C, m' = month. Plot adapted from [30]

3.4.3 Long-term ageing and phase separation

Figure 22 presents the evolution in the ϕ(T)-curves (DSC, first heating) for saturated PU9010 after exposure to water-saturated air (100% r. h.) for up to 12 months.

For the glass transition of *saturated* specimens, the GT^{cal} parameters do not change much anymore (12-month average: $T_g^{cal} = 9.3$ °C ± 0.5 K, $T_{GT\ start}^{cal} = -40.5$ °C ± 2.1 K, $T_{GT\ end}^{cal} = 32.7$ °C ± 1 K) compared to the state after short-term exposure (cf. Sect. 3.4.1, $T_g^{cal} \approx 8.7$ °C ± 0.4 K, $T_{GT\ start}^{cal} = -39.9$ °C ± 3 K, $T_{GT\ end}^{cal} = 32.6$ °C ± 2 K). Consequently, within the experimental scatter, the second stage of water uptake (starting at $t_{exposure} \approx 10$ h—cf. Sect. 3.2) does not affect the GT^{cal} in saturated PU9010. This finding confirms that water acts primarily in a physical manner in saturated PU.

For $t_{exposure} > 6$ months, the GT^{cal} parameters of *re-dried* samples (10 d at room temperature prior to DSC) are $T_g^{cal} = 25.4$ °C ± 0.6 K, $T_{GT\ start}^{cal} = -34$ °C ± 1.8 K, and $T_{GT\ end}^{cal} = 49.6$ °C ± 0.7 K after the third heating. So $T_{GT\ start}^{cal}$ and $T_{GT\ end}^{cal}$ tend to decrease slightly with respect to the juvenile material ($T_g^{cal} = 25.8$ °C ± 0.7 K, $T_{GT\ start}^{cal} = -26.7$ °C ± 4.7 K, and $T_{GT\ end}^{cal} = 51.7$ °C ± 1.7 K, cf. Sect. 3.1). Hence, with a pinch of salt, the evolving chemical degradation slightly facilitates the activation of the thermal degrees of freedom in the dry network.

Finally, an endothermic peak (at ca. -2 °C, Fig. 22) evolves from a shoulder (at ca. -6 °C), which was already mentioned for the saturated PU9010 during short-term exposure (cf. Fig. 16a). Additional DSC heating and cooling measurements (not shown) verify that the peak represents the first-order melting and freezing of a *H_2O-rich mixed phase* that the network chains form within the PU. This new phase does not consist of pure water since the melting temperature is well below 0 °C and because of the affinity between water molecules and network chains. Starting with the second stage of water uptake, this phase grows to full amount during the following 3-4 months of exposure to saturated air. The phase is detected for 100 and 95% r. h. but not for 67% r. h. and lower humidity, just like in the case for the second stage of water uptake (cf. Sect. 3.2). Obviously, the H_2O-rich PU phase only forms beyond $c_{H_2O} = 1.23$ wt%. At the same time with the evolution of the H_2O-rich phase, the samples develop optical opacity. Therefore, we attribute the phase to finely dispersed clusters in the saturated network. Re-drying fully removes the water-rich phase.

3.5 Evolution of mechanical properties of PU9010 under the influence of water

As before, only water-saturated specimens are characterised. According to Fig. 16, only the lowest $T_{test} = 26$ °C just meets the upper end of GT^{cal}. $T_{test} = 40$ and 60 °C fall into the entropy elastic range. As for the juvenile state, the isotropic compressible neo-Hooke law (Eq. 9) is applied to the range of damage-free deformation. Within experimental error, the Poisson ratio, $\nu(T_{test})$, is the same for dry and saturated PU.

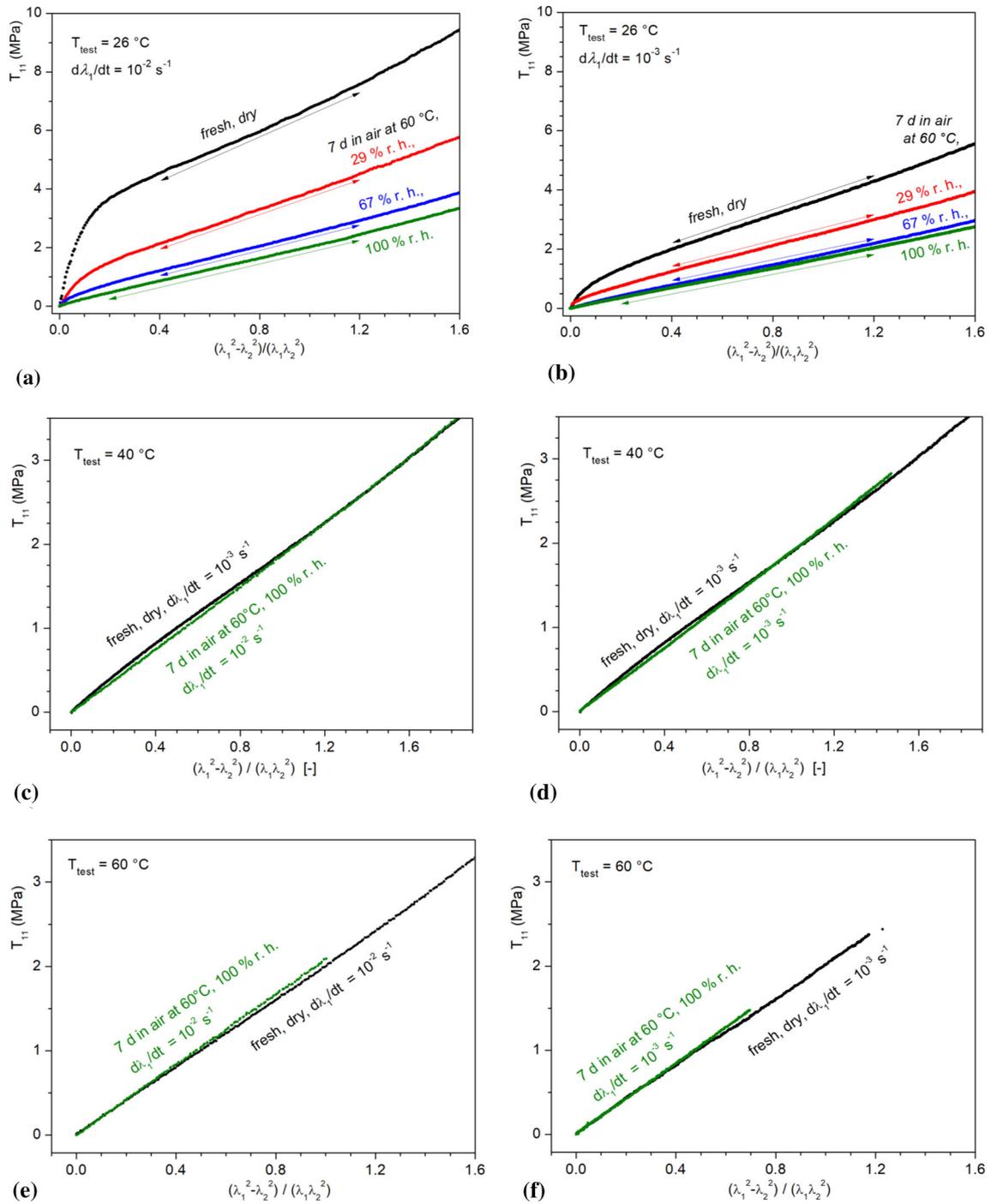**Fig. 23** Neo-Hooke plots of the tensile stress, T_{11}, at $\dot{\lambda}_1 = 10^{-2}\,\text{s}^{-1}$ and 10^{-3}s^{-1}, respectively, for saturated samples after short-term exposure to humid air versus juvenile PU9010. **a, b** $T_{test} = 26°C$, **c, d** $T_{test} = 40°C$, **e, f** $T_{test} = 60\,°C$. The coloured arrows mark the range for shear modulus determination according to neo-Hooke's law—Eq. (9). Raw data for juvenile PU9010 and for 100% r. h. from [39], plots adapted from [30]
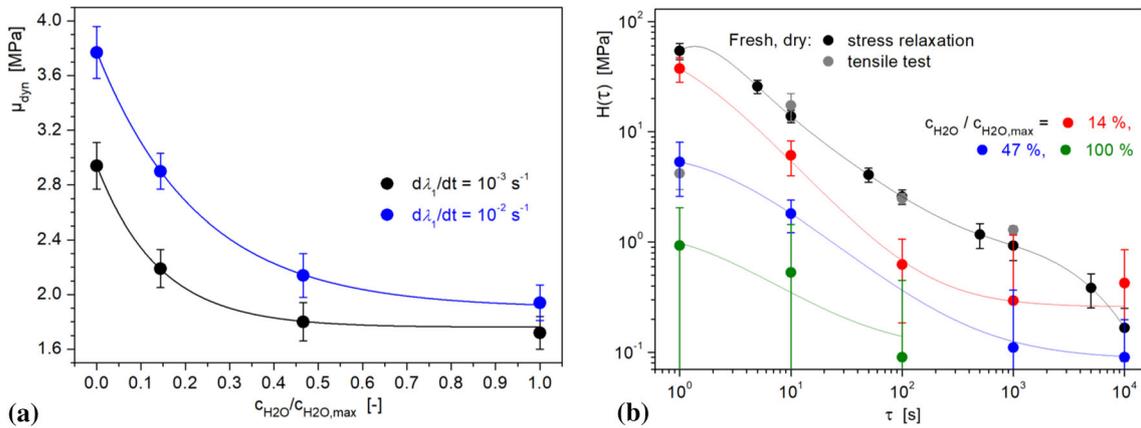
Fig. 24 a Dynamic shear modulus, $\mu_{\mathrm{dyn}}(c_{H2O})$, at $T_{\mathrm{test}} = 26\,°C$. **b** The discrete stress relaxation spectra, $H(\tau)$, as calculated by Eqs. (6, 8) for PU9010 saturated in air (60°C, various levels of humidity) from tensile tests ($T_{\mathrm{test}} = 26°C$, $\dot{\lambda}_1 = 10^{-3}\,s^{-1}$, $\dot{\lambda} = 1 \ldots 1.25$) versus the spectrum for the juvenile material (including the force relaxation values from Fig. 7). Lines as guide for the eye. Raw data for juvenile PU9010 and for 100% r. h. from [39], plots adapted from [30]

3.5.1 Stiffness

For *short-term aged*, saturated samples (i.e. the first stage of water uptake, cf. Sect. 3.2), Fig. 23 shows typical tensile curves as an example. The true tensile stress, T_{11}, is presented in the neo-Hooke plot as a function of the corresponding strain measure $\left(\frac{\lambda_1^2 - \lambda_2^2}{\lambda_1 \cdot \lambda_2^2}\right)$, as calculated from the data measured for λ_1 and λ_2.

For 26 and 40°C, any water content reduces the dynamic stiffness. At first glance, that finding clearly verifies a plasticising effect of water, but things are worth a closer look. Plasticisation is strongest for $T_{\mathrm{test}} = 26°C$ where, in addition, viscoelasticity is still present (see the curve bending in the early stage of deformation and the rate effect for the straight parts—Fig. 23a, b). Figure 24a documents the corresponding strong decrease in the dynamic modulus, μ_{dyn}, with rising water content.

The stress relaxation spectra, $H(\tau)$, explain the reason for that dramatic loss of dynamic stiffness: with rising water content, the relaxator strength values decrease by orders of magnitude in the explored relaxation time window (Fig. 24b). Hence, these mechanical relaxations wear off, while the faster relaxations (τ below the exploration window) gain influence—the H_2O molecules accelerate the molecular mobility of the network chains.
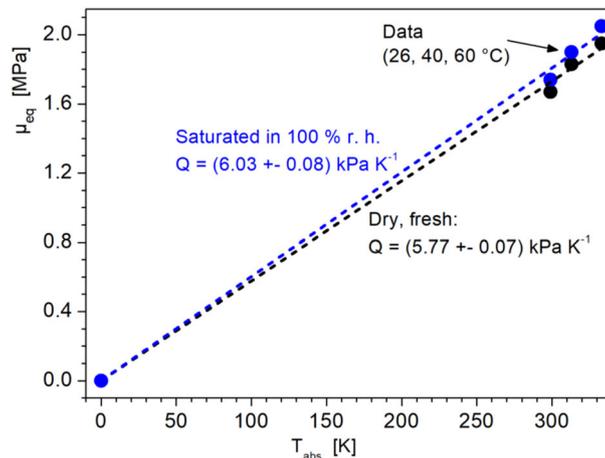

Fig. 25 Equilibrium shear modulus, $\mu_{\mathrm{eq}}(T_{\mathrm{test}})$, at $\dot{\lambda}_1 = 10^{-3}\,s^{-1}$ for PU9010 saturated with $c_{H2O,max}$ (blue dots, after 7 d in air, 100% r. h., 60°C) versus data for the juvenile dry material (black dots, including the value from force relaxation at 26°C). Raw data from [39,42]. Dashed lines = linear regression according to Eq. (11) with a very good $R^2 = 0.999$ (colour figure online)

At $T_{test} > 26\,°C$, the neo-Hooke plot gives straight lines from the start for both $\dot{\lambda}_1$ for all water saturation levels—Fig. 23 cf. Viscoelasticity disappears in the saturated PU9010 with rising T_{test} because temperature is another factor that expedites molecular mobility. Figure 25 presents the corresponding data for the *equilibrium* shear modulus, $\mu_{eq}(T_{test})$, for saturated PU9010 (air, 100% r. h., 60 °C) from tensile tests in comparison with the data for the juvenile state. For this first stage of water uptake, the $\mu_{eq}(T_{test})$-data are slightly but systematically *larger* than for the juvenile state. Moreover, water raises the parameter Q, relating to the 'effective' cross-link density in the saturated network, i.e. the presence of the H_2O molecules around the network chains affects their equilibrium deformation under external load.

At the first glance, these findings surprise since the literature on rubber elasticity (like [75,76]) and polymer textbooks depict plasticisation as a general decrease in stiffness. For explanation of our findings, we refer to the reorganisation observed for part of the urethane H-bonds (Sect. 3.4.2) by the H_2O molecules and to the concomitant gain of conformational entropy (Sect. 3.4.1). That indicates an extension of the conformational space accessible for the network due to a forced molecular mobility, and it goes with an increase in the specific conformational entropy, s_{conf}. Now, isothermal mechanical deformation results in an entropy change

$$\Delta s = s_{deformed} - s_{undeformed} < 0 \qquad (15)$$

which contributes to the specific mechanical work, w, done on the sample

$$w = \frac{1}{m_{sample}} \int T_{11} dV_{sample} = (h_{deformed} - h_{undeformed}) - T\,(s_{deformed} - s_{undeformed}) = \Delta h - T \cdot \Delta s \qquad (16)$$

h = specific enthalpy.

For rubber elasticity, we have $\Delta h \to 0$ and thus $w = -T \cdot \Delta s > 0$. As μ_{eq} is larger for saturated than for dry PU (cf. Fig. 25), we get $w_{saturated} > w_{dry}$ and $|\Delta s_{saturated}| > |\Delta s_{dry}|$. This result backs the explanation as a water-induced stimulation of the molecular mobility in the network.

During long-term ageing (100% r. h., 60 °C, up to 1 year), μ_{dyn} approaches μ_{eq} after 1 month, i.e. viscoelasticity vanishes. Further, a very small decrease in μ_{eq} (3–4%) evolves for $t_{age} > 6$ months. In view of this time line, the formation of the dispersed H_2O-rich phase is not responsible for that decrease in μ_{eq} on the long term. We assume that it is the beginning chemical degradation, which reduces the density of chemical cross-links in the network and hence of the entropy elastic modulus. More experiments are needed for the final proof of this interpretation.

3.5.2 Fracture parameters

As seen in Fig. 26 for specimens exposed to 100% r. h. at 60 °C, both fracture stretch, λ_1^{fract}, and stress, T_{11}^{fract}, respond massively to the ingressing water within hours and reach their final values with saturation. During long-term ageing (up to 1 year), the situation does not change anymore.
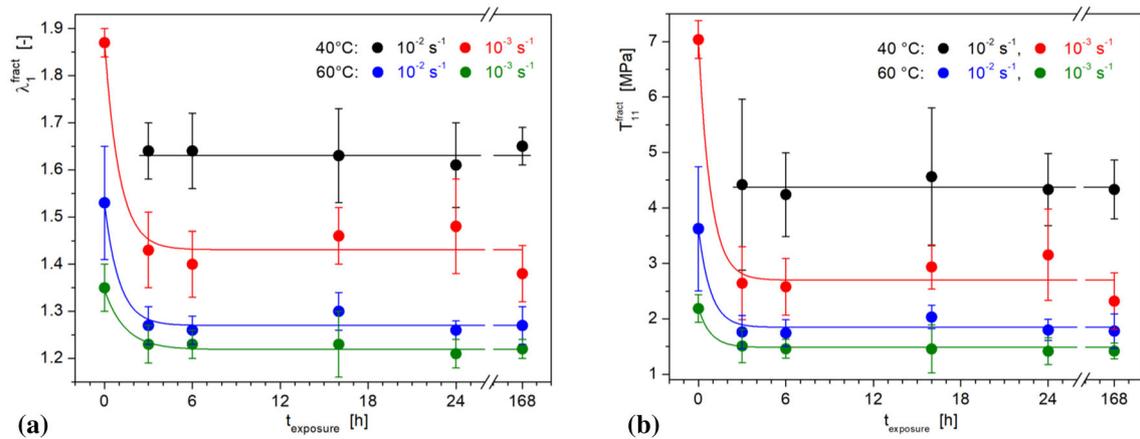

Fig. 26 Strain (**a**) and stress at fracture (**b**) of PU9010 at various T_{test} and $\dot{\lambda}_1$ during water uptake at 60 °C in 100% r. h. air. For $T_{test} = 26\,°C$, the samples break beyond the observable stretch window. Raw data from [39], plots adapted from [30]

The strong impact of T_{test}, $\dot{\lambda}_1$ and water uptake on the fracture toughness is evident. Regarding T_{test} and $\dot{\lambda}_1$, these adverse trends are characteristic for dry polymers in the viscoelastic and rubber elastic states [77,78]. Accordingly, the viscoelastic dissipation of deformation energy is made responsible: with rising test temperature, the molecular cooperative motions become faster, and smaller deformation rates give more time to these motions to relax. Hence, fracture proceeds with less energy provided from outside during the mechanical test. Similarly, we believe that the deleterious effect of water on fracture toughness should be due to the facilitated molecular relaxations documented in Sects. 3.4.1 and 3.5.1. In addition, the H_2O molecules occupy free volume compartments in the network, and this could reduce the maximum stretch the polymer chains can have before failure. Admittedly, this cannot be the full story yet, because not much is known about the complex molecular mechanisms and processes that rule fracture in polymers, neither in dry nor in wet states.

4 Summary and conclusions

With its well-defined chemical structure, the PU9010 of this study is a representative prototype for the large and technologically important group of cross-linked amorphous poly(ether urethane) materials.

The applied mild hygro-thermal ageing (humid air, 60 °C) is close to an upper limit of application conditions, and it assures the absence of unrealistic high-temperature processes.

Fick's law of diffusion describes a first stage of water uptake of PU9010 very well (up to some 7 d). On the long term (up to 4–5 months) but only in 100% r. h., a second stage of water uptake appears.

In saturated PU9010, water causes a bunch of effects, being strongest for the maximum water content obtained in contact with air of 100% relative humidity.

While the network morphology shields the residual isocyanate groups from contact with H_2O molecules, they cleave network chains at uretdione and urethane groups. The first of these *two chemical ageing processes* quickly comes to the end, and it is negligible thanks to the very small uretdione concentration in PU9010. The second process develops most weakly and slowly, as expected from the empirically well-established chemical stability of poly(ether urethanes). Hence, chemical ageing plays a minor role in PU9010 for the given ageing regime.

Concerning *physical ageing* on the molecular scale, H_2O molecules break up part of the weak H-bonds between the urethane groups and replace them by H_2O–urethane hydrogen bonds within 1 d of exposure to water-saturated air. Without doubt, the H_2O molecules also reduce all other physical interactions between network chains because they solvate hydrophilic segments. As the consequence, the macromolecular mobility strongly activates, and the gain of specific conformational entropy doubles across the caloric glass transition, which shifts downwards by $\sim$17 K. Surprisingly, a water concentration of only $c_{H2O} \approx (0.4 \ldots 0.5)\, c_{H2O,max}$ suffices for the major part of these rearrangements. Some part of the water slowly (during 3–4 months) forms a new H_2O-rich mixed phase with the PU chains, which finely disperses in the network.

Except the new phase, these molecular processes of physical ageing strongly affect the mechanical properties of PU9010.

In the limits of damage-free deformation, the neo-Hooke law for compressible isotropic media applies very well—in the rubber elastic state as well as for steady deformation in the viscoelastic range (dynamic glass transition). Hence, the corresponding *equilibrium* and *dynamic* shear moduli, $\mu_{eq}(T)$ and $\mu_{dyn}(T)$, and the Poisson's ratio, ν, fully characterise the mechanical properties of the PU network prior to stretch-induced damage. To the best of our knowledge, our data show for the first time that, after stress relaxation at temperatures in the glass transition, the modulus, $\mu_{relax}(T)$, only depends on the entropy change induced by deformation in the dry PU, i.e. $\mu_{relax}(T) = \mu_{eq}(T)$.

With the first stage of uptake, water drastically decreases the *viscoelastic* response represented by $\mu_{dyn}(T, \dot{\lambda}, c_{H2O})$, which for $c_{H2O,max}$ is only half the value of the juvenile dry PU. Similarly, in the mechanical relaxation spectrum the relaxator strength, $H(\tau, c_{H2O})$, diminishes by orders of magnitude in the explored relaxation time window. During long-term ageing, viscoelasticity vanishes in the explored temperature range (26 … 60 °C) within one month, i.e. $\mu_{dyn}(T) \rightarrow \mu_{eq}(T)$. These results document pronounced plasticisation. However, the corresponding *equilibrium* modulus, $\mu_{eq}(T)$, does just the opposite—it grows slightly in the wet material. Based on the picture that water weakens the physical inter-chain interactions, we propose an explanation for these opposite trends in dynamic and equilibrium stiffness. H_2O molecules boost the cooperative mobility in the network with respect to intensity and rate. This goes with a reduction in the energy barriers and hence with the extension of the accessible conformational space and the corresponding specific conformational entropy. In addition, the slightly higher $\mu_{eq}(T)$ in the wet PU proves that the deformation-induced specific

entropy changes are higher in the wet than in the dry state. In conclusion, for the main part water plastifies the *dynamic* mechanical response of the PU—an important result for engineering practice.

The fracture of PU9010 is a highly dynamic, energy-dissipating phenomenon. Both fracture parameters, λ_1^{fract} and T_{11}^{fract}, depend strongly on temperature and deformation rate. Water exerts a quick and most detrimental influence on these parameters. They reduce by about 50% during the first stage of water uptake before being constant for the rest of ageing. Such *embrittlement* is important for engineering practice as well. The explanation given above works for this embrittlement effect as well—the water-induced activation and acceleration of cooperative network chain motions let fracture proceed with less energy. Presumably, fast relaxations contribute most to the dynamic embrittlement. In addition, by occupying free volume compartments, H_2O molecules obstruct the elongation of network chains under mechanical load. Further research is needed to verify and detail this qualitative picture.

References

1. Chung, Y.-C., Choi, J.W., Choi, N.E., Chun, B.C.: Endurance of linear and cross-linked shape memory polyurethane under rigorous hydrolysis conditions. Fibers Polym. **10**(5), 576–582 (2009)
2. Makki, H., Adema, K.N.S., Peters, E.A.J.F., Laven, J., van der Ven, L.G.J., van Benthem, R.A.T.M., de With, G.: Quantitative spectroscopic analysis of weathering of polyester-urethane coatings. Polym. Degrad. Stab. **121**, 280–291 (2015)
3. Barendregt, R.B., Van den Berg, P.J.: The degradation of polyurethane. Thermochim. Acta **38**, 181–195 (1980)
4. de Oliviera, G.L., Gomez, A.J.A., Caire, M., Vaz, M.A., da Costa, M.F.: Characterization of seawater and weather aged polyurethane elastomer for bend stiffeners. Polym. Test. **59**, 290–295 (2017)
5. Huacuja-Sanchez, J.E., Müller, K., Possart, W.: Water diffusion in a crosslinked polyether-based polyurethane adhesive. Int. J. Adhes. Adhes. **66**, 167–175 (2016)
6. Huacuja-Sanchez, J.E., Engel, P., Possart, W.: Steel joints with a basic polyurethane adhesive—ageing processes. In: Possart, W., Brede, M. (eds.) Adhesive Joints—Ageing and Durability of Epoxies and Polyurethanes, chpt. B.5, pp. 309–348. Wiley-VCH Verlag GmbH & Co. KGaA, Weinheim (2019)
7. Kosakiewicz, J., Kozakiewicz, J., Rokicki, G., Przybylski, J., Sylwestrzak, K., Parzuchowski, P.G., Tomczyk, K.M.: Studies of the hydrolytic stability of poly(urethane-urea) elastomers synthesized from oligocarbonate diols. Polym. Degrad. Stab. **95**, 2413–2420 (2010)
8. Zain, N.M., Ahmad, S.H., Ali, E.S.: Durability of green polyurethane adhesive bonded aluminum alloy in dry and hydrothermal ageing conditions. J. Appl. Polym. Sci. **131**(23), 41151-1-41151–8 (2014)
9. Alia, C., Biezma, M.V., Pinilla, P., Arenas, J.M., Suárez, J.C.: Degradation in seawater of structural adhesives for hybrid fibre-metal laminated materials. Adv. Mater. Sci. Eng. **2013** (2013), Article ID 869075, 1–10. https://doi.org/10.1155/2013/869075
10. Aglan, H., Calhoun, M., Allie, L.: Effect of UV and hygrothermal aging on the mechanical performance of polyurethane elastomers. J. Appl. Polym. Sci. **108**(1), 558–564 (2008)
11. Boubakri, A., Elleuch, K., Guermazi, N., Ayedi, H.F.: Investigations on hygrothermal aging of thermoplastic polyurethane material. Mater. Des. **30**(10), 3958–3965 (2009)
12. Boubakri, A., Haddar, N., Elleuch, K., Bienvenu, Y.: Impact of aging conditions on mechanical properties of thermoplastic polyurethane. Mater. Des. **31**(9), 4194–4201 (2010)
13. Murata, S., Nakajima, T., Tsuzaki, N., Yasuda, M., Kato, T.: Synthesis and hydrolysis resistance of polyurethane derived from 2,4-diethyl-1,5-pentanediol. Polym. Degrad. Stab. **61**, 527–534 (1998)
14. Pretsch, T., Jakob, I., Müller, W.: Hydrolytic degradation and functional stability of a segmented shape memory poly(ester urethane). Polym. Degrad. Stab. **94**, 61–73 (2009)
15. Schoonover, J.R., Thompson, D.G., Osborn, J.C., Orler, E.B., Wrobleski, D.A., Marsh, A.L., Wang, H., Palmer, R.A.: Infrared linear dichroism study of a hydrolytically degraded poly(ester urethane). Polym. Degrad. Stab. **74**, 87–96 (2001)
16. Le Gac, P.Y., Choqueuse, D., Melot, D.: Description and modeling of polyurethane hydrolysis used as thermal insulation in oil offshore conditions. Polym. Test. **32**, 1588–1593 (2013)
17. Chaffin, K.A., Chen, X., McNamara, L., Bates, F.S., Hillmyer, M.A.: Polyether urethane hydrolytic stability after exposure to deoxygenated water. Macromolecules **47**(15), 5220–5226 (2014)

18. Fambri, L., Pegoretti, A., Kolarik, J., Gavazza, C., Penati, A.: Thermal stability of different polyurethanes after hydrolytic treatment. J. Therm. Anal. Calorim. **52**, 789–797 (1998)
19. Matuszak, M.L., Frisch, K.C., Reegen, S.L.: Hydrolysis of linear polyurethanes and model monocarbamates. J. Polym. Sci. Polym. Chem. Ed. **11**, 1683–1690 (1973)
20. Mazzu, A.L., Smith, C.P.: Determination of extractable methylene dianiline in thermoplastic polyurethanes by HPLC. J. Biomed. Mater. Res. **18**, 961–968 (1984)
21. Simon, J., Barla, F., Kelemen-Haller, A., Farkas, F., Kraxner, M.: Thermal stability of polyurethanes. Chromatographia **25**(2), 99–106 (1988)
22. Pissis, P., Apekis, L., Christodoulides, C., Niaounakis, M., Kyritsis, A., Nedbal, J.: Water effects in polyurethane block copolymers. J. Polym. Sci. B Polym. Phys. **34**(9), 1529–1539 (1996)
23. Yang, B., Huang, W.M., Li, C., Li, L.: Effects of moisture on the thermomechanical properties of a polyurethane shape memory polymer. Polymer **47**(4), 1348–1356 (2006)
24. Mondal, S., Martin, D.: Hydrolytic degradation of segmented polyurethane copolymers for biomedical applications. Polym. Degrad. Stab. **97**, 1553–1561 (2012)
25. Müller, W., Pretsch, T.: Hydrolytic aging of crystallizable shape memory poly(ester urethane): Effects on the thermo-mechanical properties and visco-elastic modeling. Eur. Polym. J. **46**, 1745–1758 (2010)
26. Pegoretti, A., Fambri, L., Penati, A., Kolarik, J.: Hydrolytic resistance of model poly(ether urethane ureas) and poly(ester urethane ureas). J. Appl. Polym. Sci. **70**(3), 577–586 (1998)
27. Ramani, K., Verhoff, J., Kumar, G., Blank, N., Rosenberg, S.: Environmental durability of moisture-cured urethane adhesive joints. Int. J. Adhes. Adhes. **20**(5), 377–385 (2000)
28. Weller, B., Wünsch, J.: Transparente Klebstoffe für Glas-Metall-Verbindungen. Stahlbau **82**(S1), 169–183 (2013)
29. Xie, F., Zhang, T., Bryant, P., Kurusingal, V., Colwell, J., Laycock, B.: Degradation and stabilization of polyurethane elastomers. Prog. Polym. Sci. **90**, 211–268 (2019)
30. Zimmer, B.: Hygrothermale Alterung amorpher Polyurethannetzwerke, Dissertation, Saarland University, Saarbrücken (2022)
31. Desmophen 3600Z, Product data sheet, Covestro AG (2015)
32. Baygal K55, Product data sheet, Covestro AG (2015)
33. Baygal K55, Safety data sheet, Covestro AG (2015)
34. Desmophen 3600Z, Safety data sheet, Covestro AG (2015)
35. Operating instruction Analytical balance KERN ABS/ABJ: Product data sheet. KERN & Sohn GmbH, Balingen-Frommern, Germany (2010)
36. Willian, T.: Wasserdiffusion in einem Zeolith-gefüllten Epoxid aus feuchter Luft, Bachelor thesis, Saarland University, Saarbrücken (2018)
37. Zhang, P.: Schädigungsverhalten von Elastomeren im Zugversuch, Master thesis, Saarland University, Saarbrücken (2017)
38. Gsell, M.: Einfluss des Wassers auf die mechanischen Eigenschaften von Epoxid-Bulkproben, Master thesis, Saarland University, Saarbrücken (2016)
39. Kick, A.: Wasser in Polyurethan mechanische, thermische und chemische Wirkung, Master thesis, Saarland University, Saarbrücken (2019)
40. Wehlack, C.: Chemische Struktur und ihre Entstehung in dünnen Epoxid- und Polyurethanschichten auf Metallen, Dissertation, Saarland University, Saarbrücken (2008)
41. Sokrates, G.: Infrared and Raman Characteristic Group Frequencies. Tables and Charts, 3rd edn. Wiley, New York (2006)
42. Barth, L.: Untersuchung des Deformationsverhaltens von Polyurethan im Vorbruchbereich, Bachelor thesis, Saarland University, Saarbrücken (2020)
43. Neuhaus, S.: Methoden zur experimentellen Untersuchung und Modellierung des Schädigungsverhaltens von Polyurethan in Spannungsrelaxationsversuchen, Master thesis, Saarland University, Saarbrücken (2018)
44. McClung, A., Gyaneshwar, P.T., Jeffery, W.B.: Strain rate- and temperature-dependent tensile properties of an epoxy-based, thermosetting, shape memory polymer (Veriflex-E). Mech. Time-Depend. Mater. **2012**(16), 205–221 (2012)
45. Pandini, S., Pegoretti, A.: Time, temperature, and strain effects on viscoelastic Poisson's ratio of epoxy resins. Polym. Eng. Sci. **48**(7), 1434–1441 (2008)
46. Crank, J.: The Mathematics of Diffusion, 2nd edn. Oxford University Press, Oxford (1995)
47. Atkins, P., de Paula, J.: Physikalische Chemie, 4th edn. Wiley-VCH, Weinheim (2006)
48. Koltzenburg, S., Maskos, M., Nuyken, O.: Polymere in Lösung, Polymere: Synthese, Eigenschaften und Anwendungen, 2nd edn. Springer, Berlin (2014)
49. Dolmaire, N., Espuche, E., Méchin, F., Pascault, J.-P.: Water transport properties of thermoplastic polyurethane films. J. Polym. Sci. B Polym. Phys. **42**, 473–492 (2004)
50. Anderson, R.B.: Modifications of the Brunauer, Emmett and Teller equation. J. Am. Chem. Soc. **68**(4), 686–691 (1946)
51. Despond, S., Espuche, E., Domard, A.: Water sorption and permeation in chitosan films: Relation between gas permeability and relative humidity. J. Polym. Sci. B Polym. Phys. **39**, 3114–3127 (2001)
52. Zhang, Z., Britt, I., Tung, M.: Water absorption in EVOH films and its influence on glass transition temperature. J. Polym. Sci. B Polym. Phys. **37**, 691–699 (1999)
53. Zimm, B., Lundberg, J.: Sorption of vapors by high polymers. J. Phys. Chem. **60**, 425–428 (1956)
54. Zimmer, B., Nies, C., Schmitt, C., Paulo, C., Possart, W.: Chemistry, polymer dynamics and mechanical properties of a two-part polyurethane elastomer during and after crosslinking. Part II: moist conditions. Polymer **149**, 238–252 (2018)
55. Szycher, M.: Szycher's Handbook of Polyurethanes. CRC Press, London (1999)
56. Zimmer, B., Nies, C., Schmitt, C., Possart, W.: Chemistry, polymer dynamics and mechanical properties of a two-part polyurethane elastomer during and after crosslinking. Part I: dry conditions. Polymer **115**, 77–95 (2017)
57. Zimmer, B.: Vernetzung und Stabilität eines reaktiven PU-Systems: dielektrische und IR-Spektroskopie, Master thesis, Saarland University, Saarbrücken (2016)

58. Camargo, R.E., Macosko, C.W., Tirrell, M., Wellinghoff, S.T.: Hydrogen bonding in segmented polyurethanes: band assignment for the carbonyl region. Polym. Commun. **24**, 314–315 (1983)
59. Coleman, M.M., Lee, K.H., Skrovanek, D.J., Painter, P.C.: Hydrogen bonding in polymers. 4. Infrared temperature studies of a simple polyurethane. Macromolecules **19**(8), 2149–2157 (1986)
60. Garrett, J.T., Xu, R., Cho, J., Runt, J.: Phase separation of diamine chain-extended poly(urethane) copolymers: FTIR spectroscopy and phase transitions. Polymer **44**(9), 2711–2719 (2003)
61. Marcos-Fernandez, A., Lozano, A.E., Gonzalez, L., Rodriguez, A.: Hydrogen bonding in copoly(ether-urea)s and its relationship with the physical properties. Macromolecules **30**, 3584–3592 (1997)
62. Sung, C.S., Schneider, N.S.: Infrared studies of hydrogen bonding in toluene diisocyanate based polyurethanes. Macromolecules **8**(1), 68–73 (1975)
63. Sung, C.S., Schneider, N.S.: Temperature dependence of hydrogen bonding in toluene diisocyanate based polyurethanes. Macromolecules **10**(2), 452–458 (1977)
64. Sung, C.S., Smith, T.W.: Properties of segmented polyether poly(urethane ureas) based on 2,4-toluene diisocyanate. 2. Infrared and mechanical studies. Macromolecules **13**, 117–121 (1980)
65. Teo, L., Chen, C., Kuo, J.: Fourier transform infrared spectroscopy study on effects of temperature on hydrogen bonding in amine-containing polyurethanes and poly(urethane urea)s. Macromolecules **30**, 1793–1799 (1997)
66. Yilgör, E., Yurtsever, E., Yilgör, I.: Hydrogen bonding and polyurethane morphology. II. Spectroscopic, thermal and crystallization behaviour of polyether blends with 1,3-dimethylurea and a model urethane compound. Polymer **43**(24), 6561–6568 (2002)
67. Bandekar, J., Klima, S.: FT-IR spectroscopic studies of polyurethanes. Part I. Bonding between urethane C-O-C groups and the NH Groups. J. Mol. Struct. **263**, 45–57 (1991)
68. Bandekar, J., Klima, S.: FT-IR spectroscopic studies of polyurethanes. Part II. Ab initio quantum chemical studies of the relative strengths of "carbonyl" and "ether" hydrogen-bonds in polyurethanes. Spectrochim. Acta Pt. A **48**(10), 1363–1370 (1992)
69. Bandekar, J., Klima, S.: FT-IR spectroscopic studies of polyurethanes. Part III. Quantum chemical studies of the carbamate group and the urethane C-O-C hydrogen bonding in polyurethanes. J. Mol. Struct. **281**(10), 113–122 (1993)
70. Sami, S., Yildirim, E., Yurtsever, M., Yurtsever, E., Yilgor, E., Yilgor, I., Wilkes, G.L.: Understanding the influence of hydrogen bonding and diisocyanate symmetry on the morphology and properties of segmented polyurethanes and polyureas: Computational and experimental study. Polymer **55**(18), 4563–4576 (2014)
71. Zhao, X., Qi, Y.H., Li, K.J., Zhang, Z.P.: Hydrogen bonds and FTIR peaks of polyether polyurethane-urea. Key Eng. Mater. **815**, 151–156 (2019)
72. Yilgör, E., Yilgör, I., Yurtsever, E.: Hydrogen bonding and polyurethane morphology. I. Quantum mechanical calculations of hydrogen bond energies and vibrational spectroscopy of model compounds. Polymer **43**(24), 6551–6559 (2002)
73. Yilgör, E., Burgaz, E., Yurtsever, E., Yilgör, İ: Comparison of hydrogen bonding in polydimethylsiloxane and polyether based urethane and urea copolymers. Polymer **41**(3), 849–857 (1998)
74. Coleman, M.M., Skrovanek, D.J., Hu, J., Painter, P.C.: Hydrogen bonding in polymer blends. 1. FTIR studies of urethane-ether blends. Macromolecules **211**, 59–65 (1988)
75. Treloar, L.R.G.: The elasticity and related properties of rubbers. Rep. Prog. Phys. **36**, 755–826 (1973)
76. Flory, P.J., Rehner, J.: Statistical mechanics of cross-linked polymer networks II. Swelling. J. Chem. Phys. **11**(11), 521–526 (1943)
77. Retting, W.: Bruchverhalten von Hochpolymeren. Kolloid Z. **210**(1), 54–63 (1966)
78. Cristiano, A.: Fracture by cavitation of model polyurethane elastomers, Dissertation, Université Pierre et Marie Curie, Paris (2009)